Effect of bubble deformation on the properties of bubbly flows

By BERNARD BUNNER[1] AND GRÉTAR TRYGGVASON[2]

[1]Cytonome, Inc., Watertown, MA 02472, USA

[2]Mechanical Engineering Department, Worcester Polytechnic Institute, Worcester, MA 01609-2280, USA

Direct numerical simulations of the motion of 27 three-dimensional deformable buoyant bubbles in periodic domains are presented. The full Navier–Stokes equations are solved by a parallelized finite-difference/front-tracking method that allows a deformable interface between the bubbles and the suspending fluid and the inclusion of surface tension. The Eötvös number is taken as equal to 5, so that the bubbles are ellipsoidal, and the Galileo number is 900, so that the rise Reynolds number of a single bubble in an unbounded flow is about 26. Three values of the void fraction have been investigated: 2%, 6% and 12%. At 6%, a change in the behaviour of the bubbles is observed. The bubbles are initially dispersed homogeneously throughout the flow field and their average rise Reynolds number is 23. After the bubbles have risen by about 90 bubble diameters, they form a vertical stream and accelerate. The microstructure of the bubble suspension is analysed and an explanation is proposed for the formation of these streams. The results for the ellipsoidal bubbles are compared to the results for nearly spherical bubbles, for which the Eötvös number is 1 and the Galileo number is 900. The dispersion of the bubbles and the velocity fluctuations in the liquid phase are analysed.

1. Introduction

Bubbly flows are of critical importance in many industrial processes, such as boiling heat transfer, cloud cavitation in hydraulic systems, stirring of reactors, aeration in water purification, bubble columns and centrifuges in the petrochemical industry, cooling devices of nuclear reactors, and scavenging of dissolved gases in separation processes. Bubbles also play a major role in a number of natural phenomena, such as the propagation of sound in the ocean, the exchange of gases and heat between the oceans and the atmosphere, and explosive volcanic eruptions.

Engineering predictions of bubbly flows have traditionally relied on correlations of bulk properties such as the mean pressure drop, the mean flow rate, or the mean wall shear stress, which are obtained from simple scaling arguments and experimental measurements (Hetsroni 1982). The knowledge of such correlations is often sufficient for one-dimensional problems such as pipe flows. However, a more detailed knowledge of the flow field is required to predict the motion of the bubbles and the liquid in complex three-dimensional problems such as bubble columns or stirred tanks. Direct numerical simulations, where all flow scales are fully resolved, provide a complete picture of the flow field. While they have had a major impact on the current understanding of turbulence in single-phase flows, numerical difficulties

have until recently limited similar progress in multiphase flows. The main difficulties are to simulate the motion of a deformable interface and to account for the proper stress boundary conditions at the interface.

A number of authors have simulated the motion of a single bubble, usually with grids fitted to the bubble interface. For example, Ryskin & Leal (1984) computed the steady-state shape of a single clean axisymmetric bubble; McLaughlin (1996) extended that study to a contaminated bubble. Takagi & Matsumoto (1994), Miyata (1996) and Oka & Ishii (1999) performed unsteady three-dimensional simulations of the motion of a deformable bubble. The motion of a single bubble has also been addressed in a large number of experimental and analytical studies and is now fairly well understood (see Clift, Grace & Weber 1978; Fan & Tsuchiya 1990; Sadhal, Ayyaswamy & Chung 1997 for reviews).

For multiple bubbles, the literature is much more limited. Some progress has been achieved by the use of simplified models. Boundary-integral techniques were used in the Stokes flow limit by Manga & Stone (1993) for gas bubbles in very viscous liquids and in the inviscid limit by Chahine (1994) for cavitating bubbles. Using the results of Moore (1965), who showed that the flow around a spherical bubble at high Reynolds number can be considered inviscid and irrotational except in a thin boundary layer and wake, Smereka (1993), Sangani & Didwania (1993) and Yurkovetsky & Brady (1996) developed techniques to simulate the motion of large numbers of spherical bubbles in the potential flow limit. These authors found that the velocities of the bubbles become equal over time and that the bubbles form horizontal rafts as they rise. The discrepancy between these findings and experimental observations, probably due to the absence of wakes in the simulations, has led workers to question the appropriateness of the potential flow assumption in dynamic simulations of bubbly liquids. Another common simplification is to assume that the bubbles can be represented as point particles (see, for example, Spelt & Biesheuvel 1997). Semi-empirical relations must be prescribed for the forces exerted by the liquid on the bubbles and these relations are only applicable in a limited region of the parameter space. In addition, direct bubble/bubble interactions are not accounted for, so that the simulations are restricted to low void fractions.

A number of methods have been developed in the past twenty years to perform direct numerical simulations of multiphase flows at finite Reynolds numbers, where inertia, viscosity, interface deformation, and surface-tension effects are all included. A review of these methods is given in Tryggvason *et al.* (2001). Hu (1996) and Johnson & Tezduyar (1997) used unstructured moving-grid techniques to simulate up to 1000 solid particles; the flow field must be remeshed at every time step to follow the motion of the particle boundaries. Simulations of fluid particles, i.e. bubbles and drops, usually rely on one-field formulations, where a single Navier–Stokes equation is solved in the entire flow field on a stationary grid and the front, or interface between the fluids, is either captured or tracked. The advantages of a one-field formulation over a moving grid are reduced computational cost and increased facility to model complex geometries and topologies. We note that a one-field approach was adopted by Glowinski *et al.* (1999) to simulate 504 solid particles in two dimensions. The volume-of-fluid and level set methods are examples of front-capturing methods. In the volume-of-fluid method (see Scardovelli & Zaleski 1999, for a review), a marker function is advected with the velocity of the flow field and the front is reconstructed at each time step from this marker function. In the level set method (Sussman & Smereka 1997), a distance function is advected with the velocity of the flow field and the front is defined as the surface where the distance function is zero. The main challenge in front-capturing

methods is to prevent two bubbles or drops from 'numerically coalescing' when their distance becomes less than one grid step. The numerical method used in this paper is a front-tracking method, where the interface is tracked explictly by a moving deformable mesh, which makes it possible to keep the bubbles separate even when they are very close.

Esmaeeli & Tryggvason (1996, 1998, 1999) used this method to simulate the motion of homogeneous bubbly flows in periodic cells. Most of the results were confined to two-dimensional systems, but a few simulations of three-dimensional systems with up to eight bubbles were also examined. Using an implementation of the same method on parallel computers, Bunner & Tryggvason (1999a; 2002a, b) simulated the motion of up to 216 nearly spherical bubbles in a three dimensional periodic cell. Bunner & Tryggvason (2002a) studied the dependence of the results on the number of bubbles. It was found that the rise velocity is predicted well by systems containing relatively few bubbles, but the fluctuation velocities and the dispersion coefficients depend strongly on the number of bubbles in the periodic cell. An analysis of the microstructure in Bunner & Tryggvason (2002a) showed a preference for an horizontal alignment of pairs of spherical bubbles. The hydrodynamic dispersion of the bubbles was found to be Gaussian to a good approximation, with strongly anisotropic diffusion coefficients. In the densest case, at a void fraction of 24%, the formation of horizontal rafts of bubbles, which periodically break up and reform, was observed. Bunner & Tryggvason (2002b) found that the velocity fluctuations induced in the liquid by the bubble motion increased with the void fraction, and that the isotropic kinetic energy spectrum followed a power law with a slope of approximately -3.6 at high wavenumbers.

In this paper, we present results from simulations of strongly deformable bubbles in homogeneous flows. Whereas previous numerical studies of bubbly flows dealt almost exclusively with nearly spherical bubbles, flows encountered in industrial applications or in nature are often composed of strongly deformed bubbles. For a given gas and a given liquid, deformation depends on the size of the bubble (Clift *et al.* 1978). For example, a clean air bubble in water is approximately spherical if its equivalent diameter is smaller than 2 mm. As the diameter increases, the bubble progressively deforms into an ellipsoid, and eventually adopts a spherical cap shape. The rise velocity increases with the diameter, although not uniformly. For example, the rise velocity actually decreases when the bubble becomes large enough that path instability sets in. In this paper, we chose the same parameters for the ellipsoidal bubbles as for the spherical bubbles, the only difference being the surface tension, which is five times lower for ellipsoidal bubbles than it is for spherical bubbles. The simulations correspond therefore to a different combination of gas and liquid. There are two reasons for this choice. First, the current numerical scheme and the currently available computer resources make it difficult to do large-scale three-dimensional simulations at high Reynolds numbers. Secondly, as a result of our choice of parameters, the rise velocities of the spherical and ellipsoidal bubbles are approximately the same, which allows us to make easier comparisons between the results for the spherical bubbles and the results for the ellipsoidal bubbles.

The main motivation for this paper is the numerical study of the rise of a deformable bubble in a vertical shear flow by Ervin & Tryggvason (1997). In agreement with the experiments of Kariyasaki (1987), Ervin & Tryggvason (1997) found that the lift coefficient depends strongly on the deformation of the bubble. Specifically, whereas the lift coefficient of a spherical bubble is positive, the lift coefficient of a strongly deformed bubble is negative. In a vertical shear flow, a spherical bubble migrates

therefore towards the region of downward velocity, while a deformable bubble migrates towards the region of upward velocity. The same results were obtained numerically and experimentally by Tomiyama *et al.* (1995).

Another motivation for this paper is the experiments of Stewart (1995), Schlüter & Räbiger (1998), Brücker (1999*a*, *b*) and Sommerfeld (personal communication 1999). Using recently developed measurement techniques, these authors measured the paths of many large, strongly deformed bubbles moving in a cluster or swarm. In a cluster of a few bubbles, Brücker (1999*a*) observed that the bubbles interact by wake drafting and continually trade places in a leapfrog fashion. If the cluster has a large number of bubbles, Stewart (1995) observed that the bubbles 'formed a chimney in which a cluster's wake was strong enough to sustain itself by continually gathering in new bubbles to replace those that dispersed outward at the top.' As noted by Schlüter & Räbiger (1998), the resulting mean rise velocity of the bubbles in the cluster is considerably larger than the rise velocity of a single bubble. This contrasts with experimental correlations (Ishii & Zuber 1979) and analytical studies (van Wijngaarden 1993), which both predict that the mean rise velocity of the bubbles decreases monotonically as the void fraction increases.

The paper is organized in the following manner. Section 2 states the problem and § 3 describes the numerical method. The formation of a stream and the microstructure of the flow are analysed in §4.1 for the case where the void fraction is 6%. The results for the ellipsoidal bubbles are compared with the results for spherical bubbles. The effect of void fraction is described in §4.2, with simulations at void fractions of 2% and 12%. The deformation and orientation of the bubbles are examined in §4.3. The dispersion process of the bubbles is characterized in §4.4. The pseudoturbulence properties of the liquid phase are analysed in §4.5. Finally, the effect of initial conditions is discussed in §4.6.

2. Problem statement

We consider the three-dimensional motion of a triply periodic monodisperse array of buoyant bubbles with equivalent diameter d or radius a, density ρ_b, viscosity μ_b and uniform surface tension σ in a fluid with density ρ_f and viscosity μ_f. The array of bubbles is repeated periodically in the three spatial directions with periods equal to L, so that the volume of the computational domain is $\Omega = L^3$. In addition to the acceleration due to gravity, g, a uniform acceleration is imposed on the fluid inside and outside the bubbles to compensate for the hydrostatic head, so that the net momentum flux through the boundaries of the computational domain is zero.

A single bubble of light fluid rising in an unbounded flow is usually described by the Eötvös number (sometimes also called the Bond number), $Eo = \rho_f g d^2 / \sigma$ and the Morton number, $M = g \mu_f^4 / \rho_f \sigma^3$ (see Clift *et al.* 1978). For given fluids, the Eötvös number is a characteristic of the bubble size and the Morton number is a constant. Instead of the Morton number, we prefer to use the Galileo or Archimedes number, $N = \rho^2 g d^3 / \mu^2 = Eo^{3/2} / M^{1/2}$, which is a Reynolds number squared based on the velocity scale $(gd)^{1/2}$. In this paper, we choose $Eo = 5$ and $N = 900$ ($M = 1.543 \times 10^{-4}$). This Morton number corresponds to a light machine oil at a temperature of about 50°C ($\mu_f = 0.0247\,\mathrm{N\,s\,m^{-2}}$, $\rho_f = 880\,\mathrm{kg\,m^{-3}}$, $\sigma = 0.03\,\mathrm{N\,m^{-1}}$ and $g = 9.81\,\mathrm{m\,s^{-2}}$) and the Eötvös number corresponds to a bubble with a diameter of about 4.2 mm. For the somewhat more interesting case of an air bubble in water, the Galileo number is usually much higher, but current computational capabilities make the study of a three-dimensional system of multiple bubbles in water difficult. An air bubble in

water with $Eo = 5$ assumes an ellipsoidal shape with a ratio of large axis length over small axis length of about 2.2 in a pure system according to the Vakrushev and Efremov correlation (Fan & Tsuchiya 1990), and a rise Reynolds number of about 1500 (Clift *et al.* 1978, chap. 7). For comparison, the corresponding values in an impure system are 1.3 and 1150 (Clift *et al.* 1978, chap. 7). Such bubbles exhibit a complex unsteady motion characterized by wobbling and rocking, vortex shedding, and shape oscillations (Lunde & Perkins 1998). In contrast, for $Eo = 5$ and $N = 900$, a single bubble follows a steady rectilinear motion. From the results of numerical simulations of Ryskin & Leal (1984), its rise Reynolds number can be estimated to be 26.3 ± 2 and its ratio of major axis length to minor axis length is 1.6 ± 0.2. This is consistent with the crude estimate that can be obtained from correlations of experimental data, which is $Re = 27.3$ (Clift *et al.* 1978, p. 176).

The fluids are taken to be free of contaminants in the simulations, so that the tangential stress is continuous across the interface. The ratios of the densities and viscosities, ρ_b/ρ_f and μ_b/μ_f, are two additional dimensionless parameters. These ratios are very small in most bubbly flows. (The density ratio for air bubbles in water is 1/800 for example.) For computational reasons, the simulations were performed at a higher value, $\rho_b/\rho_f = \mu_b/\mu_f = 1/50$. Jan (1994), Bunner & Tryggvason (2002a) and Oka & Ishii (1999) showed that this leads to negligible differences in the results.

At the initial time, the N_b bubbles are placed inside the periodic cell corresponding to the computational domain and arranged in a regular array. The position of each bubble is then perturbed slightly in each direction by a random amount chosen so that neighbouring bubbles do not intersect. The initial location of the bubbles can thus be described as a perturbed regular array. For spherical bubbles, Bunner & Tryggvason (2002a) showed that the initial configuration of the bubbles has no effect on the steady-state results. In contrast, it will be seen in §4.6 that the initial configuration of the ellipsoidal bubbles has a considerable effect on the evolution of the flow.

As they rise, the bubbles move into the other periodic cells in the vertical direction through buoyancy and in the horizontal direction through dispersion. The bubbles are not allowed to coalesce, so that N_b is constant. A fifth dimensionless parameter of this problem is the void fraction, or volume fraction of the bubbly phase, $\alpha = N_b \pi d^3/6L^3$. Since both fluids are assumed to be incompressible, α is constant throughout a simulation. The number of bubbles, N_b, is an additional parameter. Because of computational cost, only simulations with $N_b = 27$ were performed. A study of system size effects for spherical bubbles (Bunner & Tryggvason 2002a) showed that the average rise velocity of the bubbles depends only slightly on N_b for $N_b \geqslant 12$, while the velocity fluctuations of the bubbles and the liquid are more strongly affected by N_b.

Following Ishii & Zuber (1979), the drift velocity is used to present the results of the bubble velocities in the vertical direction. The drift velocity of bubble l is defined as the volume averaged velocity of bubble l minus the volume averaged velocity of the whole mixture: $W_d^{(l)}(t) = W_b^{(l)}(t) - [\alpha W_b(t) + (1-\alpha)W_f(t)]$. In this definition, $W_b^{(l)}(t)$ is calculated by taking the time derivative of the path of the barycentre of bubble l (Bunner & Tryggvason 2002a), $W_b(t)$ is the average value of $W_b^{(l)}(t)$ over all bubbles, and $W_f(t)$ is the average velocity of the liquid,

$$W_f(t) = \frac{1}{\Omega_f} \int_{\Omega_f} w(t)\,\mathrm{d}V,$$

where $\Omega_f = (1-\alpha)\Omega = (1-\alpha)L^3$ is the volume of the liquid and $w(t)$ is the vertical velocity of a liquid particle. The average drift velocity satisfies $W_d(t) = (1-\alpha)W_r(t)$,

where $W_r(t) = W_b(t) - W_f(t)$ is the relative or slip velocity between the gas phase and the liquid phase. We define the instantaneous velocity fluctuation in the vertical direction based on the instantaneous velocity fluctuation of the barycentre as

$$W_b'(t) = \left[\frac{1}{N_b} \sum_{l=1,N_b} \left(W_b^{(l)}(t) - W_b(t) \right)^2 \right]^{1/2},$$

and the time averaged velocity fluctuation in the vertical direction as

$$\langle W_b' \rangle = \frac{1}{T} \int_T W_b'(t) \, \mathrm{d}t,$$

where T is the time interval defined in table 1. An alternative choice of definition for $W_b'(t)$ would be to use the time-averaged velocity of bubble l,

$$\left[\frac{1}{N_b} \sum_{l=1,N_b} \left(W_b^{(l)}(t) - \langle W_b^{(l)} \rangle \right)^2 \right]^{1/2},$$

where $\langle W_b^{(l)} \rangle = \frac{1}{T} \int_T W_b^{(l)}(t) \, \mathrm{d}t$. The two definitions lead to values of the time-averaged velocity fluctuations that are within approximately 1% of each other in simulations that are statistically steady state, but the former definition is more appropriate in situations where the motion of the bubbles is not statistically steady throughout the simulations, as is the case for the deformable bubbles in some cases.† Similar formulae are used to define the horizontal velocity fluctuations $U_b'(t)$, $V_b'(t)$ and their time averages $\langle U_b' \rangle$ and $\langle V_b' \rangle$. Furthermore, the average values of the horizontal, or cross-stream, and the total bubble velocity fluctuations are defined as

$$\langle (U_b'^2 + V_b'^2)^{1/2} \rangle = \frac{1}{T} \int_T \left(U_b'^2(t) + V_b'^2(t) \right)^{1/2} \mathrm{d}t$$

and

$$\langle (U_b'^2 + V_b'^2 + W_b'^2)^{1/2} \rangle = \frac{1}{T} \int_T \left(U_b'^2(t) + V_b'^2(t) + W_b'^2(t) \right)^{1/2} \mathrm{d}t,$$

respectively. The bubble velocities and velocity fluctuations are presented as Reynolds numbers, using the nominal bubble diameter d as length scale and the density ρ_f and viscosity μ_f of the liquid. For example, the drift Reynolds number is $Re_d = \rho_f W_d d / \mu_f$ and the vertical fluctuation Reynolds number is $Re_{w'} = \rho_f W_b' d / \mu_f$. Their time averages are denoted by $\langle Re_d \rangle = \rho_f \langle W_d \rangle d / \mu_f$ and $\langle Re_{w'} \rangle = \rho_f \langle W_b' \rangle d / \mu_f$.

The Reynolds stresses of the liquid phase are defined as

$$(u_i' u_j')(t) = \frac{1}{\Omega_f} \int_{\Omega_f} u_i'(t) v_j'(t) \, \mathrm{d}V.$$

Here, $u_i'(t)$ stands for any of the velocity fluctuations of the liquid in the three spatial directions, $u'(t)$, $v'(t)$ or $w'(t)$, and $(u_i' u_j')(t)$ stands for any of the nine components of the Reynolds stress tensor. The time-averaged horizontal and vertical Reynolds

---

† Note that the results for the time-averaged velocity fluctuations presented in Bunner & Tryggvason (2002*a*) were calculated with the formula shown above, not with the definition shown in equation 2.16 of that paper. The two definitions lead to values that differ by less than 2% for number of bubbles greater than 27.

stresses are

$$\langle u'u' + v'v' \rangle = \frac{1}{T} \int_T ((u'u')(t) + (v'v')(t)) \, \mathrm{d}t$$

and

$$\langle w'w' \rangle = \frac{1}{T} \int_T (w'w')(t) \, \mathrm{d}t.$$

The pseudoturbulent kinetic energy is defined as $KE = (u'u' + v'v' + w'w')/2$.

3. Numerical method

The fluids inside and outside of the bubbles are taken to be Newtonian and the flow is taken to be incompressible and isothermal, so that the densities and viscosities are constant within each phase. The numerical method is based on solving the Navier–Stokes equation for the entire computational domain using a single grid and tracking the bubble surface by connected marker points. The basic numerical method, which is best described as a finite-difference/front-tracking method, is described in detail in Unverdi & Tryggvason (1992) and Tryggvason *et al.* (2001). Improvements to the basic method include the development of a numerical technique to conserve volume and parallelization of the code. The incompressibility condition results in a non-separable elliptic equation for the pressure, for which a multigrid solver was developed.

The numerical method has been validated in various ways (see Jan 1994; Esmaeeli & Tryggvason 1998). Extensive grid independence studies were reported in Bunner & Tryggvason (2002*a*) for spherical bubbles rising with approximately the same velocity as found here and were used as guidelines for the simulations of deformable bubbles. The results presented here are the bubble rise velocity W_b, the bubble velocity fluctuations U_b', V_b', W_b', the liquid velocity fluctuations, $u'u'$, $v'v'$, $w'w'$, and quantities derived from these three basic types. A grid independence study was performed for the bubble rise velocity and for the liquid velocity fluctuations. Bunner & Tryggvason (2002*a*) showed that the bubble velocity fluctuations are significantly less dependent on the grid resolution than the bubble rise velocity and the liquid velocity fluctuations, so no grid independence study was performed for the bubble velocity fluctuations in this paper.

The accuracy of the method is determined by the number of grid points across the nominal diameter of the bubble, n_d. For the parameters selected in this paper, $Eo = 5$ and $N = 900$, a resolution of at least 20.7 points per bubble diameter was adopted. A grid independence study was performed for a single bubble in a periodic domain at $\alpha = 6\%$ and $n_d = 10.7, 20.4, 31.1$ and 38.9. The plot of the drift Reynolds number and the pseudoturbulent kinetic energy of the liquid phase in figure 1 shows that the motion of the bubbles is steady after an initial transient and that a resolution of $n_d = 38.9$ leads to a solution that is essentially grid independent. The error made in using $n_d = 20.7$ instead of $n_d = 38.9$ is 2.0% for the terminal rise velocity W_T, 2.9% for the relaxation time of the rise velocity, defined as $\int (1 - W_b(t)/W_T) \, \mathrm{d}t$, 1.1% for the pseudoturbulent kinetic energy of the liquid phase, and 1.5% for the bubble deformation, defined by the ratio of major axis length over minor axis length.

While the interaction of bubbles in the range of void fractions considered in this paper is likely to lead to coalescence in some circumstances (Stewart 1995; Katz & Meneveau 1996; Duineveld 1998), we do not allow the bubbles to merge, so that statistics can be obtained for a constant number of bubbles. Although no grid refinement was done when two bubbles become close to each other, it has been shown by
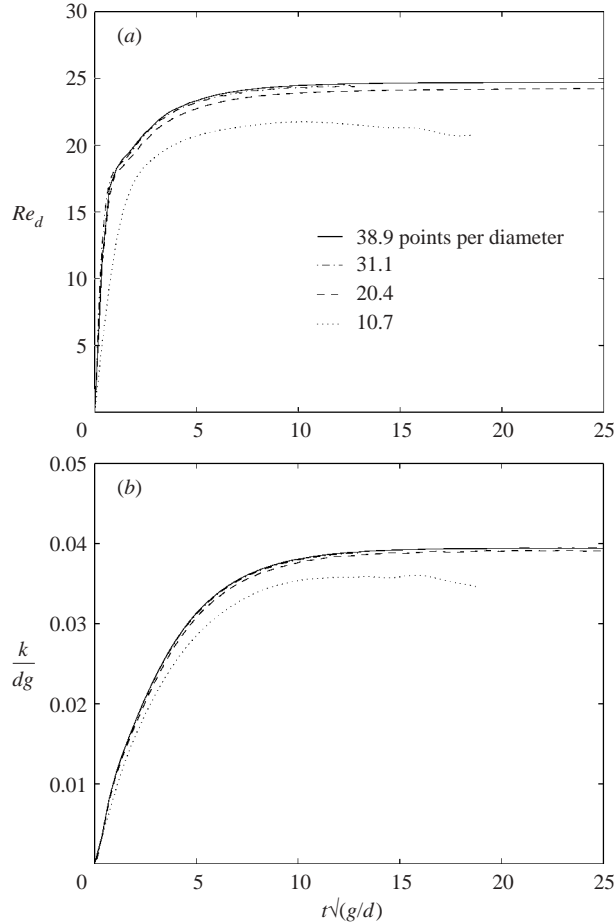
FIGURE 1. Resolution test for a regular array with $Eo = 5$, $N = 900$, $\alpha = 6\%$. (a) Drift velocity; (b) pseudoturbulent kinetic energy in the continuous phase.

Qian (1997) that our numerical method accurately accounts for the draining of the fluid film between two colliding drops, as long as the interface is fully mobile and not affected by surfactants.

4. Results

The results for deformable bubbles with Eötvös number $Eo = 5$ are compared with results from simulations with nearly spherical bubbles at $Eo = 1$ in order to highlight the strong effect of deformation on the interaction of the bubbles. The latter case has been presented in Bunner & Tryggvason (2002a, b), where results for systems with $N_b = 91$ and 216 were also included in order to study the effect of system size. For simplicity, we refer to $Eo = 5$ bubbles as either 'deformable' or 'ellipsoidal' and to $Eo = 1$ bubbles as 'spherical' in the rest of the paper, even though the latter also experience a small amount of deformation, characterized by a ratio of major axis length over minor axis length of about 1.08. $Eo = 1$ was selected rather than a smaller value of Eo because of numerical considerations. It is shown in Bunner & Tryggvason (2002a) that the motion of bubbles at $Eo = 1$ is not significantly different from that

α (%)	Eo	L/d	n_x	n_d	$T_f(g/d)^{1/2}$	$T_i(g/d)^{1/2}$	z_b/d	z_b/L	$nstep$	CPU
2	1	8.91	192	21.6	245	60	217	24.4	60720	80
2	5	8.91	192	21.6	191	40	157	19.0	49081	81
6	1	6.18	128	20.7	257	30	183	28.7	58990	79
6	5	6.18	128	20.7	184	25	179	29.0	72881	63
12	1	4.90	104	21.2	200	30	119	24.2	47710	78
12	5	4.90	104	21.2	193	30	128	26.5	69651	109

TABLE 1. List of simulations, computational parameters, and timings. L is the length of the sides of the cubic periodic domain. $n_x = n_y = n_z$ is the number of grid points in each spatial direction. n_d is the number of grid points per bubble diameter. T_f is the time at which the simulation was stopped. For all cases except $\alpha = 6\%$, $Eo = 5$, the motion of the bubbles is statistically steady and the mean values are calculated over the $[T_i, T_f]$ time interval. T_i is chosen in such a way that the initial transients are avoided. For $\alpha = 6\%$, $Eo = 5$, the mean values are calculated over the $[25, 90]$ time interval; after $t(g/d)^{1/2} \approx 90$, the motion of the system becomes unsteady. z_b is the average distance travelled by the bubbles in the vertical direction. $nstep$ is the number of time steps. CPU is the run time in days. All simulations used eight processors of an IBM SP2.

of bubbles at $Eo = 0.1$. Table 1 contains a summary of the simulations reported in this paper, along with the principal computational parameters. The simulations were performed on IBM SP2 machines at the University of Michigan's Center for Parallel Computing and at the Maui High Performance Computing Center. Generally, only one simulation was performed for each value of Eo and α. For $Eo = 1$, $\alpha = 6\%$, several simulations with different numbers of bubbles N_b and different sizes of the periodic computational domain L are reported in Bunner & Tryggvason (2002a). As mentioned in §2, the steady-state results for $Eo = 1$ are not affected by the initial conditions, although they are dependent on N_b, which prompted us to consider in this paper only simulations with the same number of bubbles, $N_b = 27$. For $\alpha = 2\%$, the effect of the initial conditions is examined in §4.6; only one simulation is considered prior to that for $Eo = 1$ and $Eo = 5$ each. It will be seen in §4.6 that initial conditions have an important effect on the development of the flow for $Eo = 5$ but not for $Eo = 1$, past an initial transient.

4.1. *Streaming of deformable bubbles*

This subsection focuses on the results of the two simulations with $\alpha = 6\%$. The drift Reynolds numbers of the 27 ellipsoidal bubbles are shown in figure 2(a). The velocity of the bubbles and the liquid is initially zero. After the bubbles are released, they experience a short transient phase where they accelerate while maintaining a nearly regular array configuration. Unlike the potential flow simulations of Smereka (1993), Sangani & Didwania (1993), and Yurkovetsky & Brady (1996), the velocities of the individual bubbles never equalize. Owing to the continual interaction of the bubbles, the rise velocities fluctuate throughout the simulations. The average drift Reynolds number of the $\alpha = 6\%$ system is shown in figure 2(b). For the spherical bubbles, $Re_d(t)$ reaches a well-defined statistical steady state after the initial transient peak. It is determined over the $[30, 257]$ time interval and is equal to 21.95. The motion of the ellipsoidal bubbles likewise settles to a statistical steady state until $t(g/d)^{1/2} \approx 90$, with an average drift Reynolds number of 21.50 over the $[25, 90]$ time interval. After this time, however, the drift Reynolds number increases steadily until $t(g/d)^{1/2} = 184$, where it reaches a value of about 50. The simulation was stopped at this time because
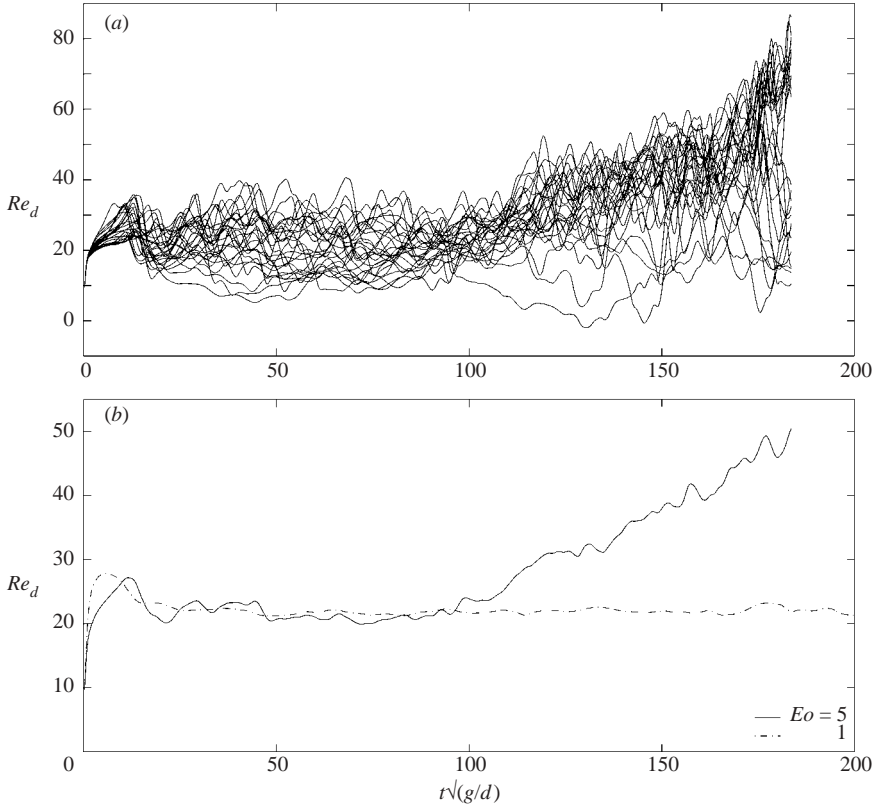
FIGURE 2. (a) Drift Reynolds number of the 27 bubbles for $\alpha = 6\%$, $Eo = 5$. (b) Average drift Reynolds number versus time for the ellipsoidal bubbles ($Eo = 5$) and the nearly spherical bubbles ($Eo = 1$).

of two numerical problems: insufficient resolution at this Reynolds number and very small time steps due to the centred finite-difference scheme. It was therefore not possible to determine the maximum value that $Re_d(t)$ would reach.

The configuration of the 27 bubbles is shown in figure 3 at $t = 88$, 128 and 177 for $Eo = 5$ and at $t = 129$ for $Eo = 1$. The streamlines and the contours of the enstrophy, $\|\boldsymbol{\omega}\|^2/2$, where $\boldsymbol{\omega} = \nabla \times \boldsymbol{u}$, are superposed in a vertical plane cross-section. The streamlines are calculated by distributing tracer particles in a plane section and integrating their motion with the velocity using the AVS visualization software. The number of tracer particles does not correspond to the number of grid points. At the early stage of the motion, the ellipsoidal bubbles are distributed approximately uniformly through the periodic cell, like the spherical bubbles, and are oriented such that their major axis is horizontal. The vorticity is larger for deformable bubbles than for spherical bubbles, since the vorticity generated at a free interface is proportional to the curvature (Batchelor 1967, §5.14). In agreement with the results of Blanco & Magnaudet (1995), no standing eddy or recirculation zone is observed behind the bubbles in this range of Reynolds number and deformation. As the rise velocity of the ellipsoidal bubbles starts increasing, a change in the structure of the flow field and in the distribution of the bubbles is seen in figure 3. The bubbles start forming a vertical stream centred around the vertical edges of the periodic domain. The location of the
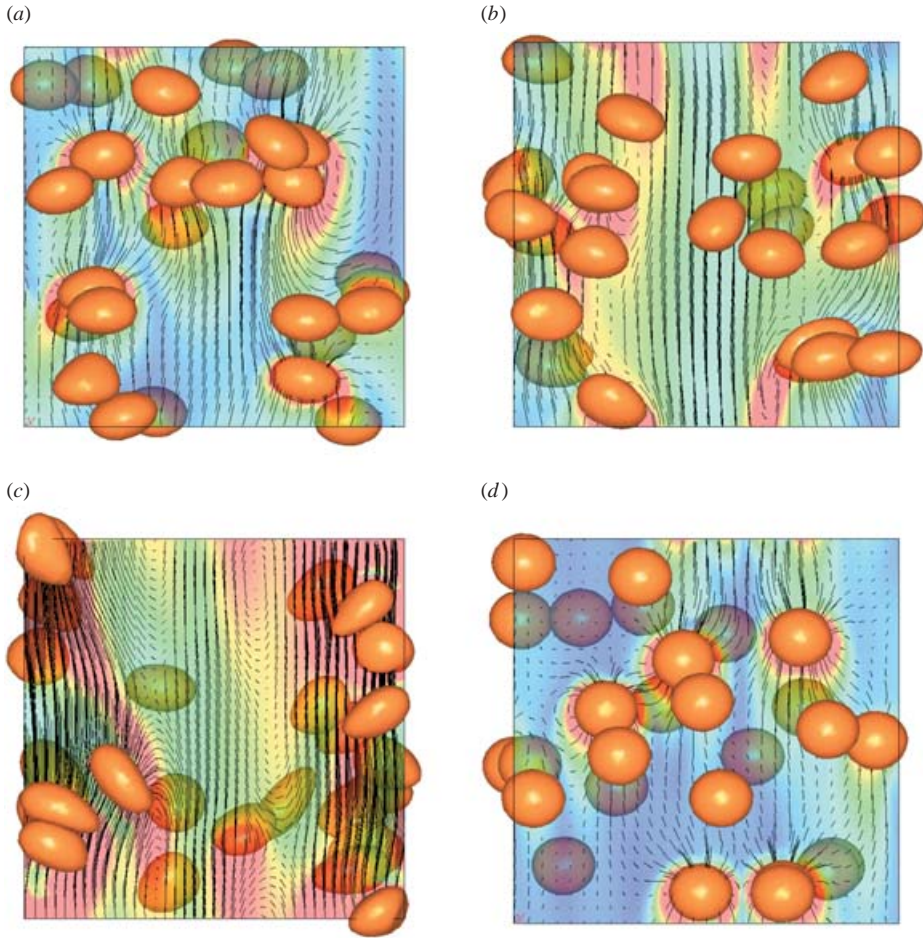
FIGURE 3. The 27 bubbles with (a) $Eo = 5$ at $t(g/d)^{1/2} = 88$, (b) 128, (c) 177, and (d) the 27 bubbles with $Eo = 1$ at $t(g/d)^{1/2} = 128$. Contours of the enstrophy, $\|\boldsymbol{\omega}\|^2/2$, where $\boldsymbol{\omega} = \nabla \times \boldsymbol{U}$, and streamlines in a plane cross-section are shown. The bubbles that are shaded lie behind the plane of the cross-section. Red and blue correspond to regions of high and low vorticity, respectively.

stream at the edges of the computational domain is not due to issues of numerical boundary conditions, as suggested by the fact that a stream also forms in the centre of the domain in §4.6. In figure 3(c), the centre of the computational domain is nearly void of bubbles. To compensate for the upward momentum of the bubbles and the liquid entrained by the bubbles, the velocity of the liquid in the centre of the domain is downward. The few bubbles located in this region are therefore slowed down and may even have negative vertical velocities (see figure 2a). Because of the larger mean rise velocity, the deformation of the bubbles increases, as discussed below in §4.3. Their shape becomes asymmetric, similar to the distorted elliptical shape seen in the deformation of a single bubble in a vertical shear flow (Ervin & Tryggvason 1997) and in the experiments of Schlüter & Räbiger (1998). In addition, the vorticity of the liquid surrounding the bubbles increases considerably.

Ervin & Tryggvason (1997) studied the motion of a single bubble in a vertical linear shear flow and found that the lift coefficient of a bubble becomes negative
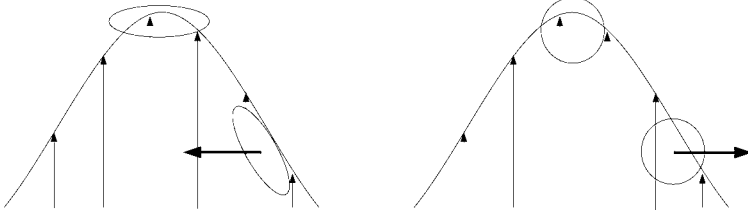
FIGURE 4. Schematic representation of a spherical and deformable bubble in the wake of another bubble. The arrows represent the direction of the lift force acting on the trailing bubble due to the local shear induced by the leading bubble. The deformable bubble moves into the wake, the spherical bubble moves away from the wake.

when the bubble deforms strongly. This provides an explanation for the streaming phenomenon, illustrated schematically in figure 4. Consider a bubble moving in the wake of one or more other bubbles. The flow field surrounding the trailing bubble has a local velocity gradient. Owing to this local shear region and the resulting lift, a spherical bubble tends to move away from the wake, whereas a deformable bubble tends to move into the wake, thus reinforcing the stream. This mechanism provides an interpretation for the qualitative differences observed between the motion of the spherical and deformable bubbles, but it does not account for the entire range of possible interactions. For example, wake effects result in the attraction of two in-line spherical bubbles if they are separated by a large distance, as was shown by Yuan & Prosperetti (1994) and as is discussed below in more details.

An increase in the rise velocity due to the interactions between deformable bubbles has also been seen in experiments (Stewart 1995; Schlüter & Räbiger 1998; Brücker 1999*a*; Sommerfeld, personal communication 1999). In particular, Schlüter & Räbiger (1998) found that the rise velocity of 4 mm diameter air bubbles in a 'swarm' of bubbles was 40% higher than the rise velocity of a single bubble in an unbounded domain. They also found that the bubbles in a swarm are more deformed than single bubbles, that their shape is asymmetric with pointed ends, and that their orientation in the swarm is such that their major axis is not horizontal. These observations are consistent with figure 3 and with §4.3.

In order to understand the microstructure of the bubble suspension, we determine the pair distribution function, which is an indicator of the probability that the distance between the centroids of two bubbles is r and that the angle between the line joining the centroids and the vertical axis is θ. More precisely, referring to figure 5 and to the notations in the caption, we consider two bubbles of centroids O and P and define the distance R and the angle Θ such that $\boldsymbol{OP} = R\boldsymbol{e}_r = \rho\boldsymbol{e}_\rho + z\boldsymbol{e}_z$ and $\Theta = \tan^{-1}(\rho/z)$. We then define the radial pair distribution function as

$$G(r) = \frac{\Omega}{N_b(N_b - 1)} \frac{1}{\Delta V(r)} \sum_{i=1,N_b} \sum_{\substack{j=1,N_b \\ i \neq j}} \delta(r - \tfrac{1}{2}\Delta r \leqslant R < r + \tfrac{1}{2}\Delta r), \qquad (4.1)$$

where $\Omega = L^3$ is the volume of the periodic cell, $\Delta V(r) = (4\pi/3)[(r + \Delta r/2)^3 - (r - \Delta r/2)^3]$ is the volume of the spherical shell of inner radius $r - \Delta r/2$ and outer radius $r + \Delta r/2$, and $\delta(x)$ is equal to one if the statement x is true and zero otherwise. In a uniform distribution of N_b points, it can be verified that $G(r) = 1$ for any value of r. Because of the finite size of bubbles, $G(r) = 0$ for $r < 2a$ if the bubbles do not deform. $G(r) < 1$ (resp. $G(r) > 1$) indicates a lower (resp. higher) likelihood of two
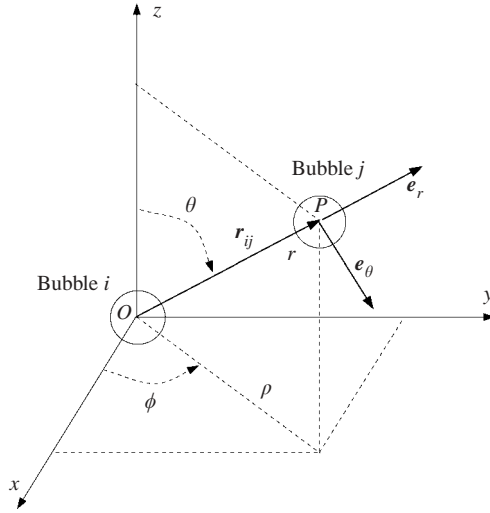
FIGURE 5. Definition of the separation vector $r_{ij} = OP$, distance r, and angle θ between bubbles i and j, and of the unit vectors $e_\rho = e_x \cos\phi + e_y \sin\phi$, $e_r = e_\rho \sin\theta + e_z \cos\theta$, and $e_\theta = e_\rho \cos\theta - e_z \sin\theta$.
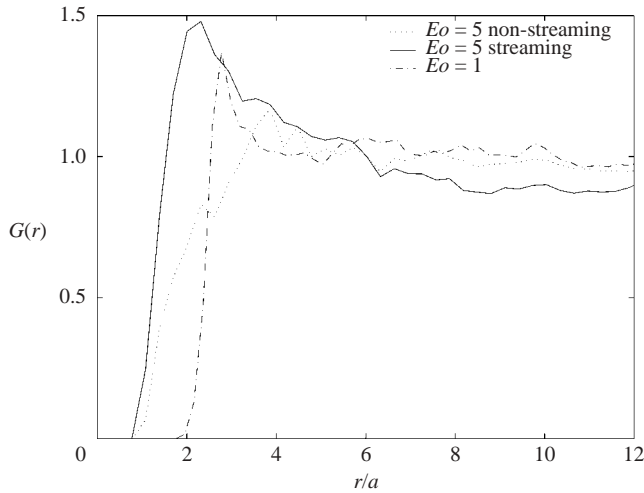

FIGURE 6. Radial pair distribution function for $\alpha = 6\%$, for the ellipsoidal bubbles ($Eo = 5$) in the non-streaming phase ($t(g/d)^{1/2} \in [25, 90]$) and in the streaming phase ($t(g/d)^{1/2} \in [100, 180]$) and for the nearly spherical bubbles ($Eo = 1$). The smallest non-zero values of $G(r)$ occur at $r = 0.8a$ for $Eo = 5$ and $r = 1.8a$ for $Eo = 1$. The horizontal axis is discretized into 40 Δr intervals. For $Eo = 5$, the results were averaged over 300 evenly spaced time samples in $[25, 90]$ (non-streaming) and 300 time samples in $[100, 180]$ (streaming). 1000 time samples were used for $Eo = 1$.

bubbles being separated by a distance r compared to a uniform distribution. The data is averaged over a large number of samples in the $[T_i, T_f]$ time intervals.

The radial pair distribution is shown in figure 6 for the deformable bubbles in the non-streaming phase ($t(g/d)^{1/2} \in [25, 90]$) and in the streaming phase ($t(g/d)^{1/2} \in [100, 180]$), and for the spherical bubbles ($t(g/d)^{1/2} \in [30, 257]$). It is important to point out that the data for $Eo = 5$ and $t(g/d)^{1/2} \in [100, 180]$ represents unsteady,

not steady-state, results, that are only averaged for convenience of presentation. We verified that the results do not change significantly when Δr is multiplied or divided by two (although the noise in the data increases when Δr becomes very small because of the finite number of samples), or when the number of time samples is increased or decreased by a factor of two. More detailed sensitivity tests are reported for spherical bubbles in Bunner & Tryggvason (2002*a*). Beside grid convergence or grid independence, it is also important to verify that the results are not affected by the limited size of the periodic domain. The effect of the number of bubbles on $G(r)$ and $G_r(\theta)$ was examined in Bunner & Tryggvason (2002*a*). While a small effect was observed, it is not sufficient to significantly alter the microstructure results, at least when the motion of the bubbles is statistically steady. When the bubbles are streaming, we are not in a position to evaluate the effect of system size on the microstructure results and on the time, at which streaming sets in.

For the spherical bubbles, a peak close to $r = 2a$ is observed, similar to corresponding results for spherical particles (Bossis & Brady 1984). Owing to the small deformation at $Eo = 1$, $G(r)$ is essentially zero for $r < 2a$. In contrast, because of the large deformation for $Eo = 5$, $G(r) > 0$ for $r > 0.8a$. In the non-streaming phase, $G(r)$ has only a small peak for the deformable bubbles and $G(r) \to 1$ as r increases, suggesting that the motion of two bubbles at large distances is uncorrelated and that the bubbles are uniformly distributed. In the streaming phase, the peak is much larger and $G(r) < 1$ for $r > 6a$, which is consistent with the fact that the bubbles are gathered in a vertical column. The non-zero values of G_r for $r < 2a$ shows that the bubbles have deformed significantly such that the minor axis is closer to a than $2a$. An inspection of figure 3 suggests that these results for $r < a$ correspond to in-line collision of the bubbles.

For a given value of r, we also define the angular pair distribution function as

$$G_r(\theta) = \frac{\Omega}{N_b(N_b - 1)} \frac{1}{\Delta V(\theta)} \sum_{i=1,N_b} \sum_{\substack{j=1,N_b \\ i \neq j}} \delta\left(\theta - \tfrac{1}{2}\Delta\theta \leqslant \Theta < \theta + \tfrac{1}{2}\Delta\theta; \ R < r\right), \quad (4.2)$$

where $\Delta V(\theta) = (2\pi r^3/3)[\cos(\theta - \Delta\theta/2) - \cos(\theta + \Delta\theta/2)]$ is the volume of the angular sector of radius r contained within the angles $\theta - \Delta\theta/2$ and $\theta + \Delta\theta/2$. In a uniform distribution of N_b points, it can be verified that $G_r(\theta) = 1$ for any value of θ and r. However, because of the finite radius of the bubbles, $G_r(\theta)$ is small when r is small and becomes larger as r increases. For example, in a uniform distribution of perfectly spherical bubbles, we would have $G_r(\theta) = 0$ for $r < 2a$ and $G_r(\theta) = (r^3 - (2a)^3)/r^3$ for $r > 2a$. To correct for this 'excluded-volume' effect, $G_r(\theta)$ is normalized so that $G_r(\theta) = 1$ corresponds to a uniform distribution of bubbles and $\frac{1}{2}\int_0^\pi G_r(\theta) \sin\theta \, d\theta = 1$. Like $G(r)$, $G_r(\theta)$ is averaged over many time samples and sensitivity tests were performed. $G_r(\theta)$ is shown in figure 7. For small values of r, $G_r(\theta)$ is indicative of the alignment of close bubble pairs. For $Eo = 5$ and $r = 2.5a$, $G_r(\theta)$ exhibits peaks close to $\theta = 0$ (bubble P is ahead of the reference bubble O) and π (bubble P is behind the reference bubble O), indicating that pairs of deformable bubbles tend to align themselves vertically. This trend is more pronounced in the streaming phase than in the non-streaming phase. For $Eo = 1$, the peak is at $\theta = \pi/2$, indicating that pairs of spherical bubbles tend to align themselves horizontally.

Additional understanding of the dynamics of the bubble interactions can be obtained by looking at the relative velocity of bubble pairs. The relative velocity of the bubble pair O, P is decomposed into its radial and tangential components along e_r and e_θ, V_r and V_θ. A simple quantitative description of the relative motion
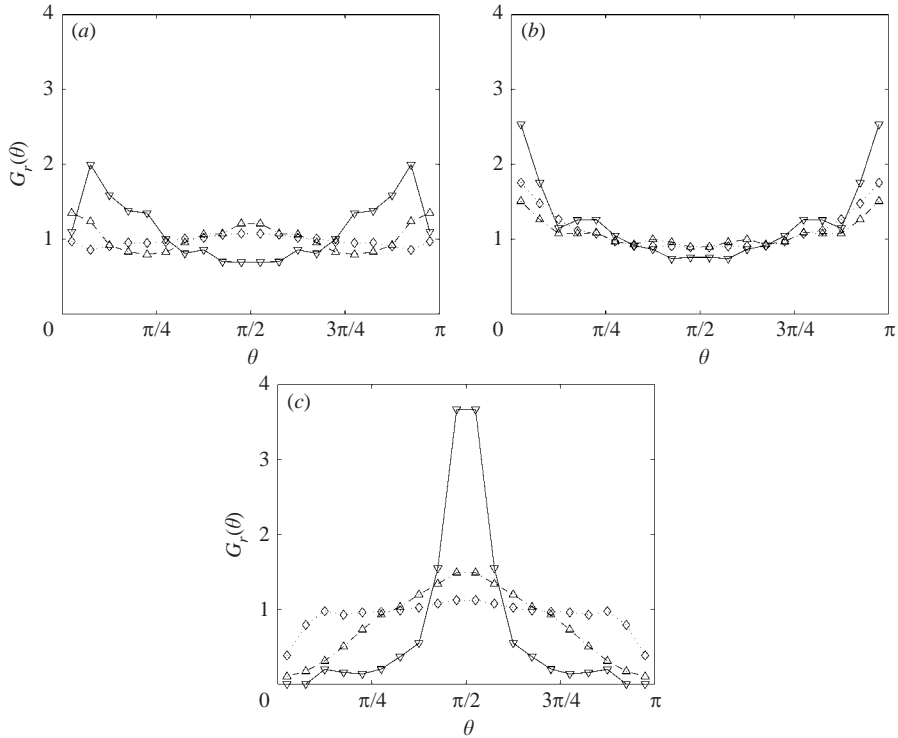
FIGURE 7. Angular pair distribution function $G_r(\theta)$ versus θ for three different values of the separation distance r. Results are shown for the ellipsoidal bubbles ($Eo = 5$) (a) in the non-streaming phase by averaging over 300 time samples in the [25, 90] time interval and (b) in the streaming phase by averaging over 300 time samples in the [100, 180] time interval. The results for the $Eo = 1$ bubbles are averaged over 1000 time samples in the [30, 256] time interval and are shown in (c). $\triangledown$, $r = 2.5a$; $\triangle$, $4.0a$; $\diamond$, $8.0a$.

of bubble pairs can be obtained by calculating the probability of V_r and V_θ being positive as functions of θ. This is done for all bubble pairs separated by a distance less than r, in the same manner as was done for $G_r(\theta)$. In a uniformly distributed suspension, $P(V_r > 0 \mid R < r) = 0.5$ and $P(V_\theta > 0 \mid R < r) = 0.5$.

$P(V_r > 0 \mid R < r)$ is shown versus θ for different values of r in figure 8. The same observations can be made for all cases. Two in-line bubbles tend to attract each other ($P(V_r > 0 \mid R < r) < 0.5$ for θ close to 0 and π). Two side-by-side bubbles tend to repel each other ($P(V_r > 0 \mid R < r) > 0.5$ for θ close to $\pi/2$). This repulsion is stronger for deformable bubbles than for spherical bubbles at a given value of r. This can be attributed both to the larger horizontal space occupied by deformable bubbles and to the larger amount of vorticity generated at their surface.

In contrast, important differences can be seen in the plots of $P(V_\theta > 0 \mid R < r)$ versus θ (figure 9) between the spherical and deformable bubbles. At $\theta \approx 0$, $P(V_\theta > 0 \mid R < r) \approx 1$ for the spherical bubbles, indicating that, when two bubbles are aligned vertically, they tend to rotate around each other toward a horizontal alignment. This is consistent with the observation made from $G_r(\theta)$ that spherical bubbles tend to align themselves horizontally with respect to their neighbours. It is also consistent with the study by Harper (1970) of two spherical bubbles rising in a vertical line in the absence of surface contamination and at high Reynolds number. Harper found that the two bubbles reach an equilibrium distance, which is stable to small vertical disturbances
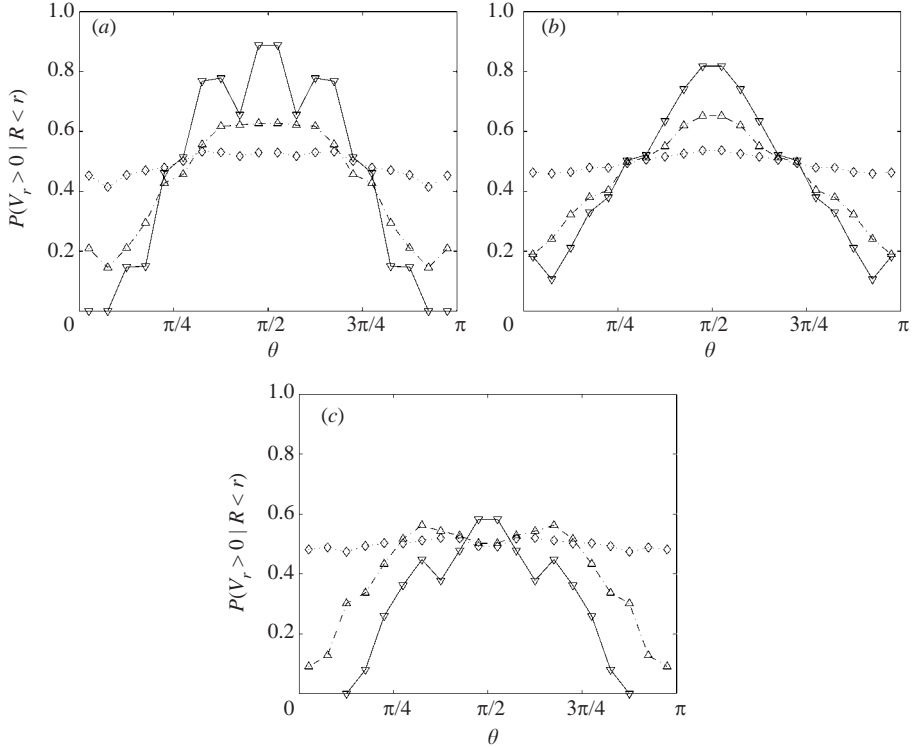
FIGURE 8. $P(V_r \geqslant 0 \mid R < r)$, the probability that the radial relative velocity between two bubbles is positive, versus θ for three different values of r. The parameters are the same as in figure 7.

but unstable to horizontal ones. When more than two bubbles are present, these disturbances are caused by the neighbouring bubbles. For the deformable bubbles, $P(V_\theta > 0 \mid R < r) \approx 0.5$ at $\theta \approx 0$, indicating that there is no tendency for two vertically aligned bubbles to rotate around each other. This is in agreement with the previous observation that deformable bubbles tend to align themselves vertically with respect to their neighbours. The results in the non-streaming and streaming phases are qualitatively similar.

In summary, the interaction of two bubbles can be described by the following sequence of events, illustrated in figure 10. If two bubbles are initially in line, the trailing bubble accelerates in the wake of the leading bubble. Two spherical bubbles rotate about each other before they collide, while two deformable bubbles remain in line until they collide, and then rotate about each other. This pairing process is similar to the 'drafting, kissing, and tumbling' mechanism identified by Fortes, Joseph & Lundgren (1987) for solid spheres sedimenting in water. The major difference between solid spheres and spherical bubbles is that the wake effect, and therefore the 'drafting' mechanism, is weaker for bubbles than for solid particles, so that a vertical alignment of spherical bubbles is less stable than a vertical alignment of solid spheres. The reason for the weaker wake effect is the lesser amount of vorticity generated at a free interface than at a no-slip boundary. As a consequence, two spherical bubbles tend to 'tumble' before they have a chance to 'kiss'. Spherical bubbles do collide with each other, as the results for $G(r)$ show, but this is due to the large void fraction, not the wake effect. In fact, we verified that spherical bubbles never touch in the more dilute case, $\alpha = 2\%$.
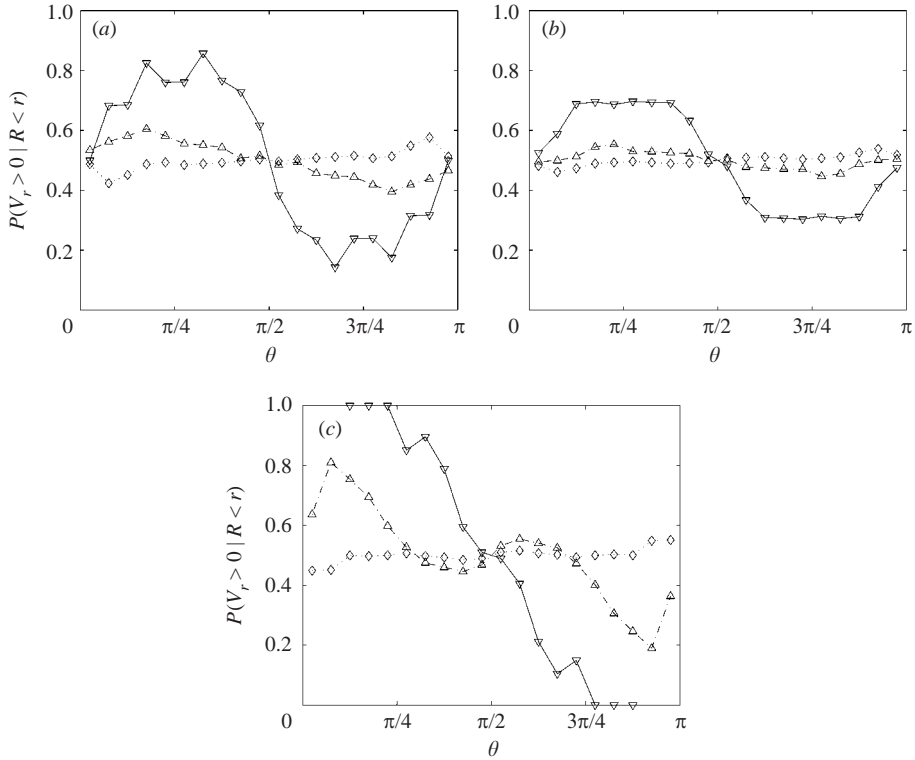
FIGURE 9. $P(V_\theta \geqslant 0 \mid R < r)$, the probability that the angular relative velocity between two bubbles is positive, versus θ for three different values of r. The parameters are the same as in figure 7.
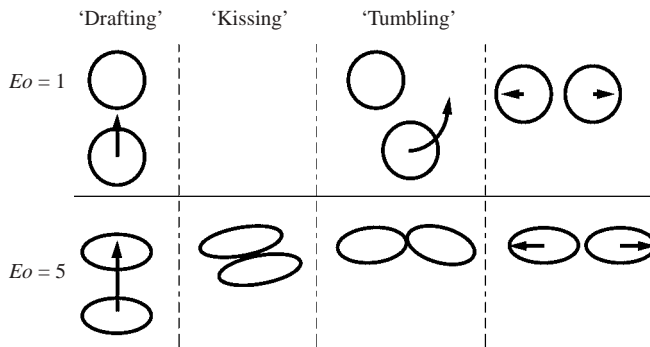

FIGURE 10. Schematic representation of the 'drafting, kissing and tumbling' sequence (Fortes *et al.* 1987).

It is interesting to look at the previous findings in light of potential flow results for the relative motion of two bubbles. In the potential flow approximation, the Reynolds number is assumed to be large enough that the flow around each bubble can be considered inviscid and irrotational, yet small enough that the bubbles do not deform significantly. Biesheuvel & van Wijngaarden (1982), Kok (1989) and van Wijngaarden (1993) showed that two in-line bubbles repel each other and that two bubbles always approach each other horizontally. This mechanism leads to the

formation of horizontal rafts of bubbles in the potential flow simulations of bubbly liquids of Smereka (1993), Sangani & Didwania (1993) and Yurkovetsky & Brady (1996). In our simulations at finite Reynolds numbers, pairs of spherical bubbles also tend to align themselves horizontally, but the interaction process is fundamentally different. Two spherical bubbles approach each other along a vertical line and then rotate into a horizontal configuration. When they are aligned horizontally, they repel, owing to the vorticity generated at the interface, as shown by Legendre & Magnaudet (1998). Since larger amounts of vorticity are generated at the interfaces of deformable bubbles, they repel faster than spherical bubbles. Legendre & Magnaudet found that two side-by-side bubbles attract each other when they are far from each other but repel when they are close, so that there exists an equilibrium distance where two side-by-side bubbles rise steadily. In potential flow theory and simulations, since vorticity is not accounted for, it is not surprising that side-by-side bubbles attract until they touch, which leads to the formation of horizontal rafts.

At finite Reynolds numbers, analysis by Harper (1997) and simulations by Yuan & Prosperetti (1994) showed that two in-line spherical bubbles attract each other owing to wake effect and repel each other owing to an adverse pressure gradient. When these two effects balance each other, the two bubbles reach an equilibrium distance, which is unstable to lateral disturbances, as noted previously. However, an equilibrium distance was not seen in the corresponding experiments of Katz & Meneveau (1996). Instead, they observed that the two bubbles always collided. They suggested that the discrepancy was due to the deformation of the bubbles in the experiments. Both the existence of an equilibrium distance for spherical bubbles and the absence of it for deformable bubbles are qualitatively consistent with our simulation results. However, for the range of parameters used by Katz & Meneveau, which is $Re_b = 0.2 - 100$ and $Eo < 0.3$, our results for $Eo = 1$ bubbles indicate that in-line bubbles should not collide. This suggests that surface deformation is not the factor responsible for the collisions observed in the experiments. The real reason might be the presence of surfactants in the experiments. Surfactants are known to have a profound effect on the behaviour of small bubbles, and especially on the amount of vorticity generated at the interface and hence the strength of the wake.

The influence of the microstructure on the rise velocity is illustrated in figure 11, where the drift Reynolds number of bubble pairs is plotted versus θ. The mean drift Reynolds number, Re_d, is represented by a solid horizontal line, except in the streaming phase, where no average rise velocity can be defined, since the motion of the bubbles is unsteady. Two in-line bubbles ($\theta \approx 0$ and $\theta \approx \pi$) rise faster than two side-by-side bubbles ($\theta \approx \pi/2$). The average velocity of a close pair of side-by-side bubbles ($r = 2.5a$ and $\theta \approx \pi/2$) is about 23 for deformable bubbles (figure 11a) and 19 for spherical bubbles (figure 11c). Since deformation increases the drag (Moore 1965) and since our results show that the side-by-side configuration minimizes the rise velocity, it seems surprising that the velocity of a pair of close side-by-side deformable bubbles is larger than both the average velocity of all bubbles, $Re_d = 21.50$, and the velocity of a pair of close side-by-side spherical bubbles. A possible explanation relies on the observation that the situation where two bubbles are very close and side-by-side is usually the result of the 'drafting, kissing and tumbling' pairing process since side-by-side bubbles usually repel. In this situation, the two bubbles are already moving fast because of the previous acceleration of the trailing bubble in the wake of the leading bubble and their subsequent collision (see also §4.3). When the two bubbles are aligned horizontally and repel, their rise velocity subsequently decreases, as seen in figure 11(a, b).
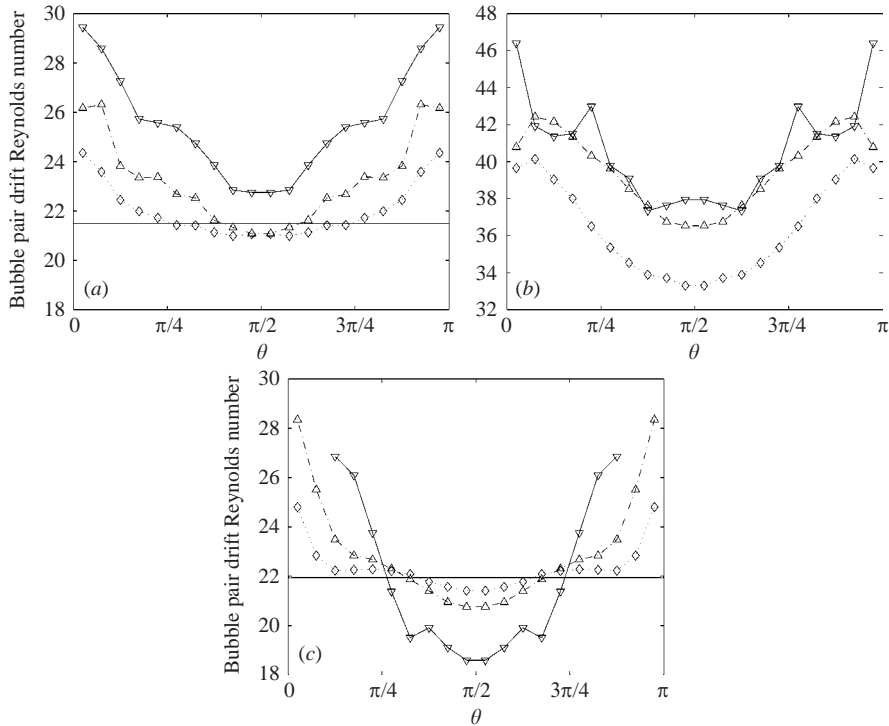
FIGURE 11. The average drift Reynolds number of pairs of bubbles as a function of θ for three different values of r. The parameters are the same as in figure 7. The horizontal lines mark the average drift Reynolds numbers, $\langle Re_d \rangle$, calculated over the [25, 90] time interval for (*a*) and the [30, 256] time interval for (*c*).
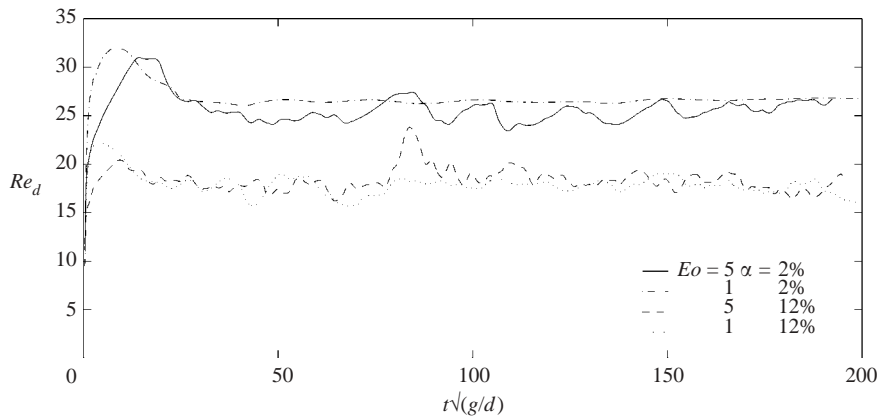

FIGURE 12. Average drift Reynolds number *vs.* time for the ellipsoidal bubbles ($Eo = 5$) and the spherical bubbles ($Eo = 1$) at $\alpha = 2\%$ and 12%.

4.2. *Effect of void fraction*

The average drift Reynolds number of the 27 ellipsoidal and spherical bubbles is shown versus time in figure 12 for $\alpha = 2\%$ and 12%. The peak in the initial transient occurs at a later time for the ellipsoidal bubbles than for the spherical bubbles, since
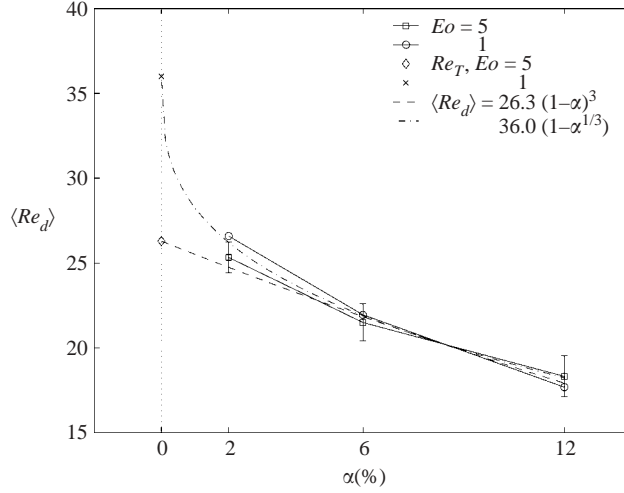
FIGURE 13. Mean drift Reynolds number as a function of the void fraction for $Eo=1$ and $Eo=5$. The terminal velocity of a single bubble in an unbounded flow, Re_T, is added for each case. Fits to the simulation results and to these terminal velocities are also shown: $\langle Re_d \rangle = 26.3\,(1-\alpha)^3$ for $Eo=5$ and $\langle Re_d \rangle = 36.0\,(1-\alpha^{1/3})$ for $Eo=1$. The point for $Eo=5$, $\alpha=6\%$ corresponds to the average of the data in the $[25, 90]$ time interval, before the streaming phase.

the wake is larger and takes longer to develop. We note that the deformation of the ellipsoidal bubbles from their initially spherical shape happens much faster than the duration of the initial transient. The system reaches a statistical steady state in all cases, characterized by larger fluctuations around the mean for the ellipsoidal than for the spherical bubbles. No streaming is observed for the deformable bubbles for $\alpha=2\%$ and $\alpha=12\%$. For $Eo=5$, $\alpha=12\%$, a small peak can be seen at $t(g/d)^{1/2} \approx 80$. A computer animation shows that the deformable bubbles start to form a stream at this time, but the stream breaks up almost immediately because the large void fraction prevents the bubbles from organizing themselves into a large-scale flow structure. For $Eo=5$, $\alpha=2\%$, it will be seen in §4.6 that the bubbles form a stable stream when they are initially placed in a vertical column. In contrast, no streaming instability is observed in figure 12, where the bubbles are initially distributed in a perturbed regular array. It is likely that a stream would form at a later time if the simulation were continued. This point is discussed further in §4.6.

The mean drift Reynolds number, Re_d, is shown versus the void fraction in figure 13. The point for $Eo=5$, $\alpha=6\%$ corresponds to the average of the data in the $[25, 90]$ time interval, before the streaming phase. In addition to the simulation results at $\alpha=2\%$, 6% and 12%, the steady rise Reynolds number of a single bubble in an infinite domain, Re_T, which corresponds to $\alpha=0$, is also shown (see §2 for $Eo=5$ and Bunner & Tryggvason 2002a for $Eo=1$). Whereas the value of Re_T of a spherical bubble, 36.0, is much larger than the value of Re_T of an ellipsoidal bubble, 26.3, the values of Re_d in the $[2\%, 12\%]$ void fraction range are within 5% of each other. For spherical bubbles, Re_d drops sharply between $\alpha=0$ and $\alpha=2\%$ owing to a change in the microstructure. A similar rapid dropoff was found in experiments at $Re \sim 200$ by van Wijngaarden & Kapteyn (1990) for bubbles that were likewise nearly spherical. The slower decrease between $\alpha=0$ and $\alpha=2\%$ for the ellipsoidal bubbles can be explained by the different interaction mechanisms between the bubbles that were
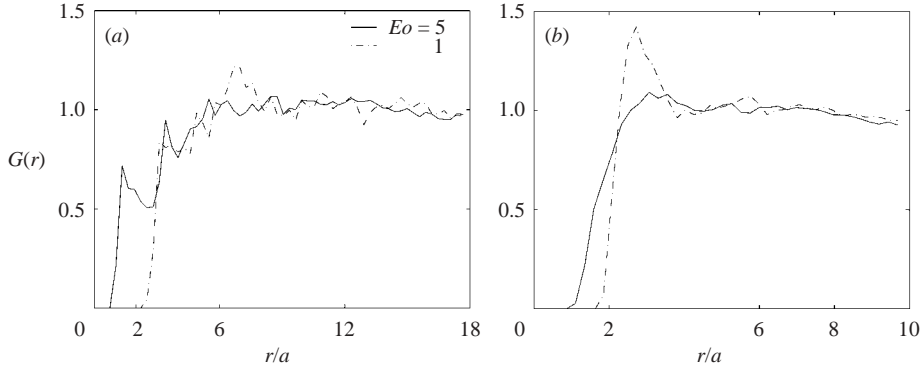
FIGURE 14. Radial pair distribution function for (*a*) $\alpha = 2\%$ and (*b*) $\alpha = 12\%$. For $\alpha = 2\%$, the smallest non-zero values of $G(r)$ occur at $r = 0.8a$ ($Eo = 5$) and $2.1a$ ($Eo = 1$). For $\alpha = 12\%$, the corresponding values are $r = 0.9a$ ($Eo = 5$) and $1.6a$ ($Eo = 1$.) The horizontal axes are discretized into, respectively, 60 and 40 Δr intervals in (*a*) and (*b*). The results are averaged over at least 500 equispaced time samples in the $[T_i, T_f]$ time interval.

discussed in §4.1. In very dilute conditions, the bubbles do not interact much. As the void fraction increases and the interactions become more important, spherical bubbles tend to align themselves in horizontal pairs, whose average rise velocity is lower than the rise velocity of isolated bubbles (Legendre & Magnaudet 1998). In contrast, deformable bubbles tend to align themselves in vertical pairs, whose rise velocity is higher than the velocity of isolated bubbles (Harper 1970; Yuan & Prosperetti 1994). As a result, even though the average velocity decreases as α increases, this decrease is slower for deformable bubbles than for spherical bubbles. The evolution of the rise velocity with the void fraction is therefore the result of the competition of the hindering effect due to other bubbles in the flow, which tends to increase the drag, and the bubble–bubble interaction mechanism, which tends to decrease the drag in the case of deformable bubbles. This is discussed further in §4.6.

Two fits to the simulation results and the Re_T points are added to figure 13. The $(1 - \alpha)^3$ power law suggested for the deformable bubbles is the experimental correlation proposed by Ishii & Zuber (1979) in this range of Reynolds number (they call it 'viscous regime'). The $(1 - \alpha^{1/3})$ relation for the spherical bubbles is a purely numerical fit.

The radial relative distribution function, $G(r)$, is shown in figure 14 for $\alpha = 2\%$ and 12%. For $Eo = 1$ and $\alpha = 2\%$, $G(r) = 0$ for $r < 2.5a$, indicating that spherical bubbles tend to stay away from each other in dilute conditions. We verified that spherical bubbles never touch at $\alpha = 2\%$ by calculating the minimum distance between the interfaces of neighbouring bubbles at each time step in the simulation. A small peak in $G(r)$ can be seen at $r \approx 7a$, consistent with the observation, also made in a computer animation of the bubbles' motion, that spherical bubbles tend to repel each other. For $Eo = 5$ and $\alpha = 2\%$, $G(r) > 0$ for $r \geqslant 0.8a$, suggesting that deformable bubbles touch and that their deformation increases when they do so. This is also seen in a computer animation of the bubbles' motion and in Bunner & Tryggvason (1999*b*). It is possible to identify a number of 'drafting, kissing and tumbling' events in the animation. This mechanism is the reason why two deformable bubbles usually come close to each other, and bubbles are rarely seen to approach each other horizontally, similarly to what Stewart (1995) observed in experiments. For $Eo = 1$ and $\alpha = 12\%$, $G(r) > 0$ for $r > 1.6a$ and has a peak at $r \approx 2.7a$. These results are similar to those found at $\alpha = 6\%$

and show that spherical bubbles collide when the void fraction is high. For $Eo = 5$ and $\alpha = 12\%$, no peak is visible, and $G(r) > 0$ for $r \geqslant 0.9a$. The minimum value of r at which $G(r) > 0$ is larger at $\alpha = 12\%$ than at $\alpha = 2\%$. This is due to the larger deformation of the bubbles at $\alpha = 2\%$ when they collide as explained below. At a void fraction of 2%, the interactions are primarily binary. A bubble which is drafted into the wake of another bubble has a large velocity relative to the leading bubble. When the two bubbles collide, the large kinetic energy of the trailing bubble translates into large deformations of both bubbles. At a void fraction of 12%, bubbles interact with many neighbours simultaneously. As a result, pairs of bubbles do not have enough time to undergo the full 'drafting, kissing and tumbling' cycle and a bubble trailing another bubble does not accelerate as much as it does at 2%, and therefore does not deform as much upon collision. Deformation is discussed further in §4.3.

$G_r(\theta)$, $P(V_r > 0 \mid R < r)$ and $P(V_\theta > 0 \mid R < r)$ for $\alpha = 2\%$ and 12% are not shown, but they exhibit the same qualitative trends as for $\alpha = 6\%$. The tendency for pairs of ellipsoidal bubbles to be aligned vertically is more pronounced when the void fraction is low. For high void fractions, vertical alignments of pairs of bubbles tend to be perturbed by the surrounding bubbles. As a consequence, the curves of the average drift Reynolds number of a pair of bubbles as a function of θ is flatter for $\alpha = 12\%$ than for $\alpha = 2\%$. For example, the difference between the values of $\langle Re_d \rangle$ at $\theta = 0$ and $\theta = \pi/2$ for $r = 4.0a$ is 8 for $\alpha = 2\%$, but only 4 for $\alpha = 12\%$ (it is 5 for $\alpha = 6\%$, see figure 11a).

4.3. *Deformation and orientation of the bubbles*

When the deformation of a bubble is small, it is usually characterized by the ratio between the longer and smaller axes (Moore 1965). Since it is not possible to measure this quantity precisely for all bubbles at all times, we define the deformation of a bubble as the square root of the ratio of the larger and smaller eigenvalues of the second moment of inertia tensor, $\chi = (I_{max}/I_{min})^{1/2}$, the second moment of inertia being defined by:

$$I_{ij} = \frac{1}{Vol_b} \int_{Vol_b} (x_i - x_{i_0})(x_j - x_{j_0}) \, \mathrm{d}V, \tag{4.3}$$

where Vol_b is the volume of the bubble and x_{i_0} and x_{j_0} are the coordinates of the bubble's centroid in the i and j directions. The volume integrals are calculated as surface integrals over the bubble interface using the divergence theorem. For a parallelepiped with sides of lengths $a > b > c$, it can be shown that $\chi = a/c$. We performed a number of tests with a single bubble in a periodic cell (a 'regular array'), where $\alpha = 6\%$, $N = 900$ and the surface tension varied such that $0.1 \leqslant Eo \leqslant 10$. We found that χ increased from 1.008 to 1.379 as Eo increased from 0.1 to 10. Since the motion of the bubble is steady for these parameters, we measured the ratio of the longer and smaller axes from plots of the bubble and found that the relative difference between the measured value and χ was less than 1.5%. For a larger deformation, $Eo = 50$, we found that $\chi = 1.585$ and that the difference between the measured value and χ was 6%. χ therefore provides a good estimate of the deformation when it is small. In addition to the deformation, the second moment of inertia tensor also allows us to define the orientation angle of each bubble as the angle ϕ between the vertical direction and the minor axis, which corresponds to the eigenvector with the smallest eigenvalue. For an oblate bubble rising in steady motion, $\phi = 0$.

Plots of the time evolution of χ and ϕ (not included) show that at $t = 0$, $\chi = 1$ since the bubbles are initially spherical, then the bubbles deform until $\chi \approx 1.4$ and accelerate without significantly interacting with their neighbours. At $t(g/d)^{1/2} \approx 10$, the initial
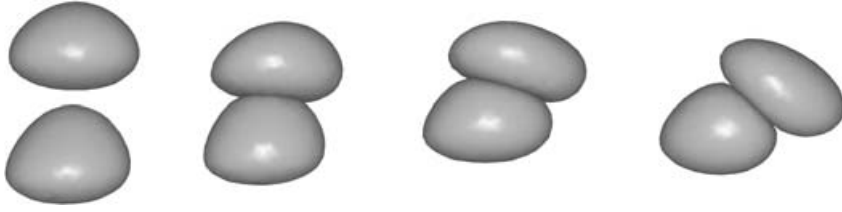
FIGURE 15. Two bubbles from the $Eo = 5, \alpha = 2\%$ simulation at times 103.0, 105.3, 106.1 and 107.0, from left to right.
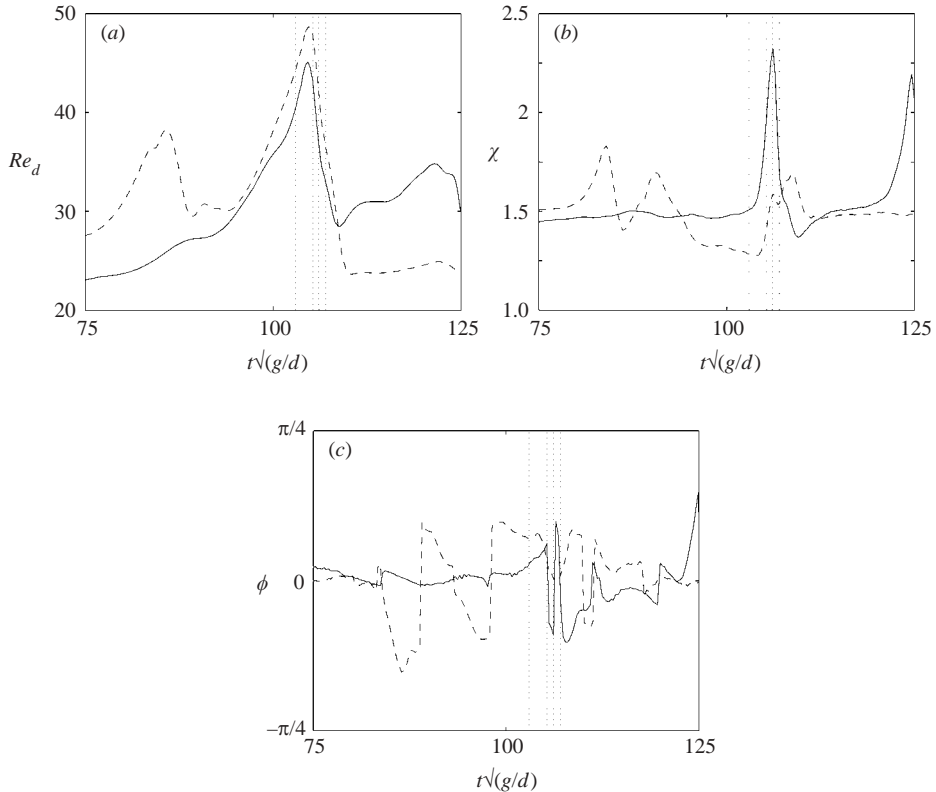

FIGURE 16. (a) Rise Reynolds number, (b) deformation, χ, and (c) orientation angle, ϕ, of the two bubbles in figure 15 versus time. ——, bubble 2 and – – –, bubble 17 are, respectively, the leading and trailing bubbles in figure 15. The vertical dotted lines denote times 103.0, 105.3, 106.1 and 107.0.

array breaks up and the bubbles start to interact strongly. χ and ϕ then fluctuate because of collisions between the bubbles. A typical interaction event is illustrated in figure 15. One bubble accelerates in the wake of a leading bubble until they collide, after which the trailing bubble pushes the leading bubble aside. The rise velocity, deformation, and orientation of these two bubbles are shown in figure 16 to study in detail the sequence of events in this 'drafting, kissing and tumbling' process. As the two bubbles come closer to each other, their rise velocities increase. Owing to the suction effect of the wake, the trailing bubble is slightly less deformed than the leading bubble. Its shape is asymmetric, with a bulge on its upper half, as seen in figure 15.
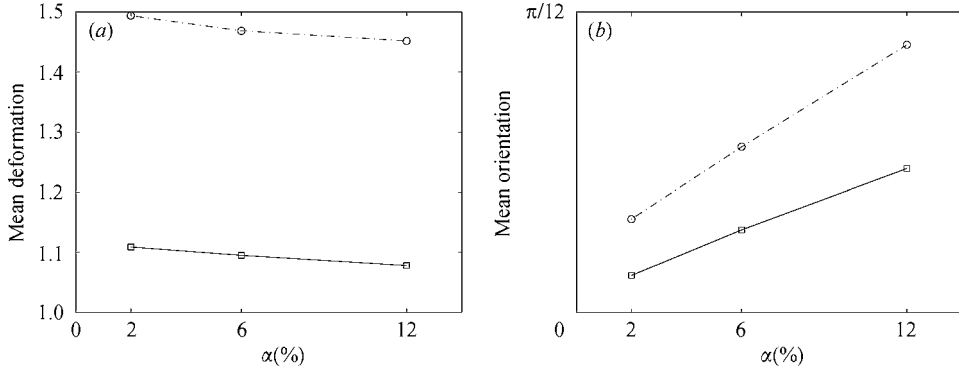
FIGURE 17. Mean (*a*) deformation, χ, and (*b*) orientation angle, ϕ, versus void fraction. The mean deformation is the average of χ over the $[T_i, T_f]$ time interval and over the 27 bubbles. The mean orientation is the average of $|\theta|$ over $[T_i, T_f]$ and over the 27 bubbles. The points for $Eo = 5$, $\alpha = 6\%$ correspond to the averages of the data in the $[25, 90]$ time interval, before the streaming phase. $\bigcirc$, $Eo = 5$; $\square$, 1.

When the two bubbles touch, their rise velocity starts decreasing and the deformation of the leading bubble increases by about 50%, as the kinetic energy of the fluid is transformed into surface energy of the bubble interface. The deformation of the trailing bubble increases also, but after a delay and to a lesser extent than that of the leading bubble. After the two bubbles have separated, their deformations experience small underrelaxations, but no shape oscillations are observed in this system, unlike in the results of experiments by Lunde & Perkins (1998), which were performed at much higher Reynolds numbers. The orientations of the bubbles in figure 16(*c*) experience sharp fluctuations around $\phi = 0$, the angle corresponding to the steady rise motion of an oblate bubble. Figure 15 illustrates a collision that is nearly on-axis and produces large increases in deformation and rise velocity. In addition, the bubbles frequently experience slightly off-axis collisions, which are characterized by smaller increases in deformation and rise velocity, or, owing to the finite void fraction, interactions with horizontal neighbours, where the bubbles repel each other.

In experimental studies of binary interactions of deformable bubbles, Stewart (1995) and Brücker (1999*b*) observed that collisions between bubbles only occurred after one bubble had been captured in the wake of another bubble. The description of the collision process in these papers is similar to the sequence of events in figure 16, with one significant difference. In the experiments, the trailing bubble did not accelerate smoothly in the wake of the leading bubble, as it does in our simulations, but in a series of jumps. The difference can be attributed to the more complicated wake structure due to the larger bubble rise Reynolds numbers of the experiments (see Brücker 1999*b* for a discussion of wake structure). Interestingly, Stewart notes that the two bubbles never coalesce during the initial collision.

The average deformation and orientation angle of the bubbles is shown versus the void fraction in figure 17. For $Eo = 5$, $\chi \approx 1.45$. For $Eo = 1$, $\chi \approx 1.10$. When α increases, the fluctuations of χ and ϕ increase as the bubbles interact more frequently and with more neighbours. However, the mean deformation decreases as α increases, as seen in figure 17(*a*). This decrease is attributable to the reduction in the rise velocity and to increased interaction of vertical pairs of bubbles, where the suction of the leading bubble leads to a bulge and therefore a smaller deformation of the trailing bubble, as seen in figure 15. For ellipsoidal bubbles, another reason is the smaller
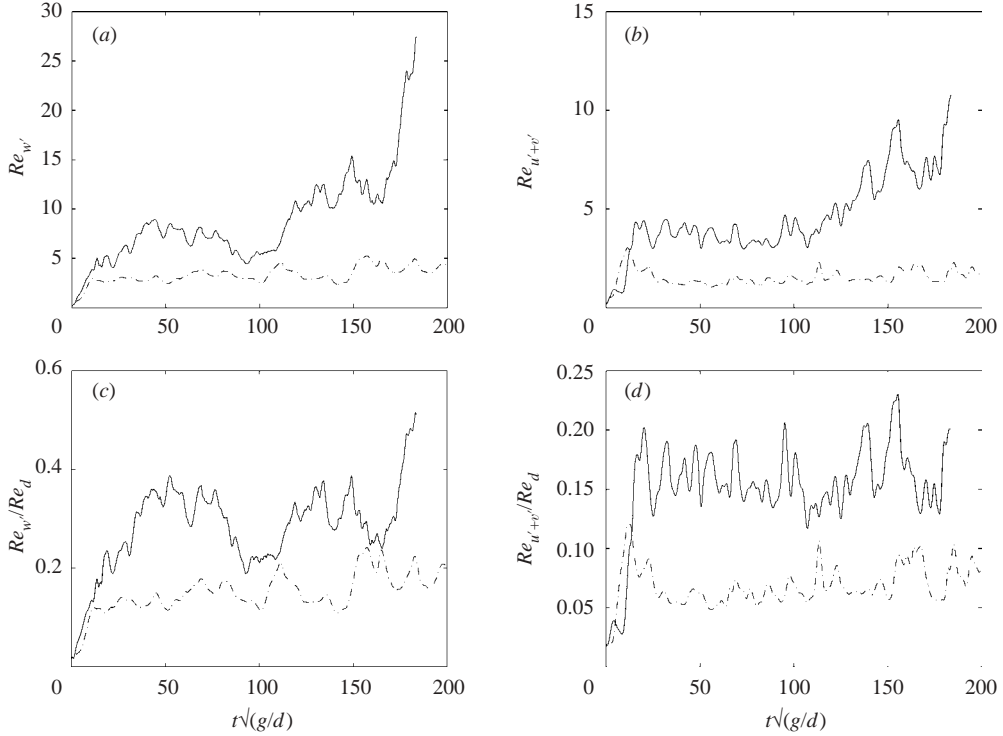
FIGURE 18. Average (*a*) streamwise and (*b*) crossstream bubble velocity fluctuations versus time for $\alpha = 6\%$. $Re_{w'} = \rho_f W_b' d / \mu_f$, $Re_{u'+v'} = \rho_f (U_b'^2 + V_b'^2)^{1/2} d / \mu_f$. In (*c*) and (*d*), the fluctuation velocities are scaled by the instantaneous drift velocities, from figure 2. ○, $Eo = 5$; —·—, 1.

differential velocity of two interacting bubbles at high void fraction than at low void fraction and, subsequently, smaller deformation upon collision. The data shown in figure 17 for $Eo = 5$, $\alpha = 6\%$ is only for the non-streaming phase. In the streaming phase, the deformation increases significantly as the bubbles' velocities increase and reaches values larger than for $\alpha = 2\%$. This data is not shown in the figure because no steady state was reached in the streaming phase. The increase of the mean orientation angle in figure 17(*b*) indicates that the angle between the vertical plane and the minor axis of the bubbles tends to increase as α increases. This is consistent with the fact that the bubbles experience larger fluctuations and more frequent interactions with their neighbours at high void fraction than at low void fraction, where $\phi = 0$ in the limit $\alpha \to 0$, since the rise motion of a single bubble in this range of Reynolds numbers is steady.

4.4. *Hydrodynamic dispersion of the bubbles*

The vertical and horizontal bubble fluctuation Reynolds numbers are shown versus time in figures 18(*a*, *b*) for $\alpha = 6\%$. While the rise velocities of the spherical and ellipsoidal bubbles are similar, the velocity fluctuations of the ellipsoidal bubbles are much larger than those of the spherical bubbles. In the streaming phase, the velocity fluctuations of the ellipsoidal bubbles increase (figure 18*a*, *b*), like the rise velocity. However, the velocity fluctuations scaled by the rise velocity (figure 18*c*, *d*) remain approximately constant, except for $t(g/d)^{1/2} > 170$, shortly before the simulation had to be stopped.
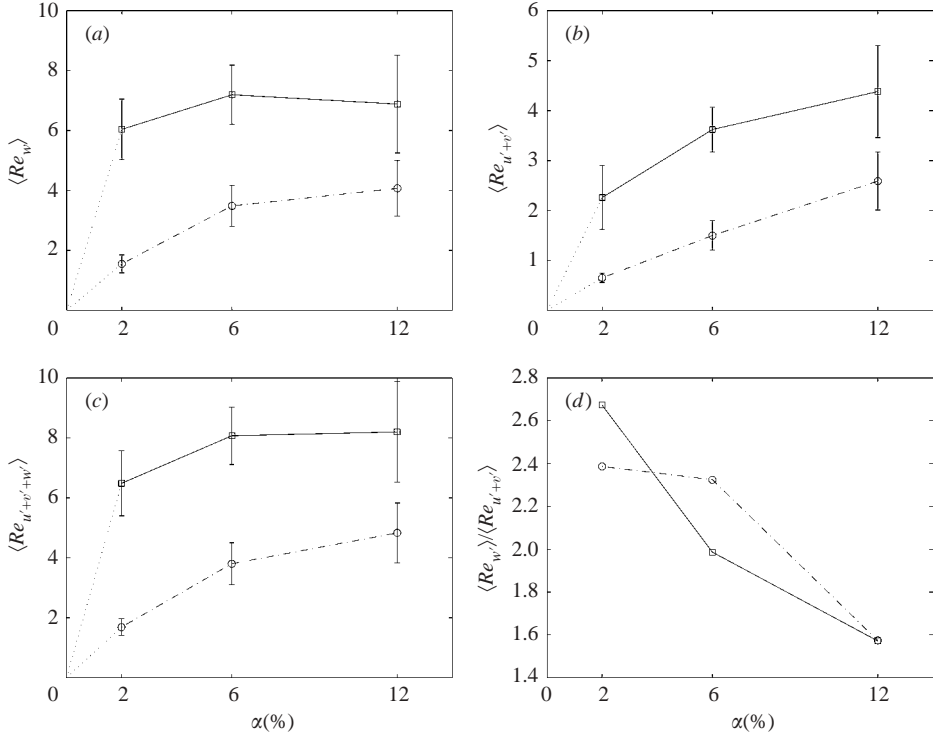
FIGURE 19. Effect of the void fraction on the bubble velocity fluctuations: (*a*) streamwise component, (*b*) cross-stream component, (*c*) total velocity fluctuations. (*d*) Ratio of the streamwise over the cross-stream components. The total velocity fluctuations are defined as $Re_{u'+v'+w'} = \rho_f (U_b'^2 + V_b'^2 + W_b'^2)^{1/2} d/\mu_f$, the other notations are as in figure 18. The points for $Eo = 5$, $\alpha = 6\%$ correspond to the averages of the data in the [25, 90] time interval, before the streaming phase. □, $Eo = 5$; ○, 1.

The mean vertical, horizontal and total fluctuation Reynolds numbers are shown in figure 19(*a–c*). The horizontal velocity fluctuations increase in the entire [2%, 12%] interval, as do the vertical velocity fluctuations of the spherical bubbles. However, the vertical velocity fluctuations of the ellipsoidal bubbles remain at about the same level between 2% and 12%. As a result, the ratio of the vertical or streamwise velocity fluctuations over the horizontal or cross-stream velocity fluctuations at $Eo = 5$ and $Eo = 1$ is about 3.9 for $\alpha = 2\%$, but only 1.7 for $\alpha = 12\%$. The velocity fluctuations are strongly anisotropic, as seen in figure 19(*d*), but the anisotropy declines too as the void fraction increases.

Bunner & Tryggvason (2002*a*) found that the variance of the spherical bubble velocities, i.e. the square of the total velocity fluctuations, followed an affine scaling with the void fraction and the rise velocity: $Re_{u'+v'+w'}^2 = 0.54\alpha Re_b^2 - 0.0069$, where $Re_{u'+v'+w'} = \rho_f (U_b'^2 + V_b'^2 + W_b'^2)^{1/2} d/\mu_f$. From figure 20, it is clear that no such scaling exists for the variance of the ellipsoidal bubbles.

Because of continual interactions between a bubble and its neighbours, two bubbles that are close at time T_0 move apart as they rise, so that the mean-square displacement of the bubbles $X_b^2(T \mid T_0)$, increases with time T. $X_b^2(T \mid T_0)$ is defined by

$$X_b^2(T \mid T_0) = \frac{1}{N_b} \sum_{l=1,N_b} \left[\Delta X_b^{(l)}(T) - \Delta X_b^{(l)}(T_0) \right]^2, \qquad (4.4)$$
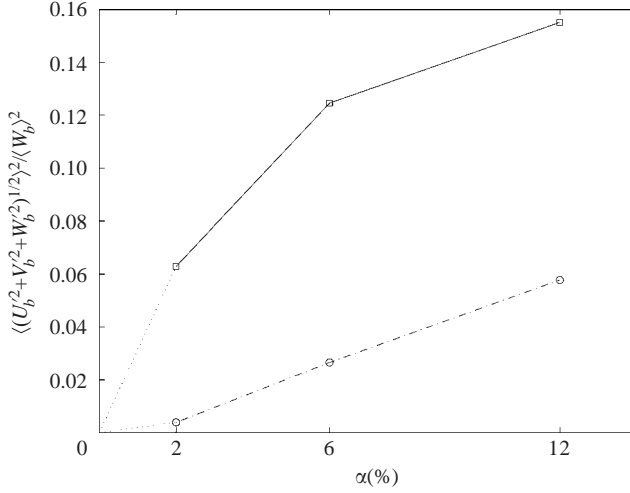
FIGURE 20. Scaling of the bubble velocity variance by the square of the mean bubble rise velocity. The point for $Eo = 5$, $\alpha = 2\%$ corresponds to the average of the data in the $[25, 90]$ time interval, before the streaming phase. $\square$, $Eo = 5$; $\bigcirc$, 1.

where $\Delta X_b^{(l)}(T) = X_b^{(l)}(T) - X_b(T)$ is the distance between the position $X_b^{(l)}(T)$ of bubble l and the barycentre of all bubbles at time T,

$$X_b(T) = \frac{1}{N_b} \sum_{l=1, N_b} X_b^{(l)}(T).$$

In all these expressions, $X_b^{(l)}(T)$ stands for the centre of mass of bubble l in any of the three spatial coordinates (see Bunner & Tryggvason 2002a for a description of how the centre of mass is defined and calculated from the position of the interface). Note that $X_b(T_0 \mid T_0) = 0$ by definition.

The hydrodynamic dispersion of the bubbles is commonly described by a diffusion model (Crowe, Troutt & Chung 1996, Sokolichin, Eigenberger, Lapin & Lübbert 1999). However, for this model to be applicable, it must be shown that the statistics of the bubble motion are Gaussian (Batchelor & Townsend 1956). To that effect, we determine the probability density function of the bubble velocity which is shown in figure 21. The values of the bubble velocities are normalized so that the p.d.f. has zero mean and would have a standard deviation of one if the statistics of the bubbles' motion were Gaussian. Bunner & Tryggvason (2002a) found that this probability density was approximately Gaussian for $Eo = 1$ and α varying from 2% to 24%. The differences between the results and the Gaussian curve are larger for ellipsoidal bubbles than for spherical bubbles. The departure from a Gaussian distribution is high at $\alpha = 2\%$, especially for U_b and V_b but is smaller at higher void fractions. The flatness factor for the results in figure 21 is between 2.6 and 5.2, whereas it is between 2.3 and 3.5 for the spherical bubbles (Bunner & Tryggvason 2002a). For $Eo = 5$ and $\alpha = 6\%$, the p.d.f. of W_b in the streaming phase is strongly asymmetric, with a peak at a positive value, while the p.d.f.'s of U_b and V_b are symmetric and their maxima are at 0. The asymmetry for W_b can be seen in figure 21(c) and explained in the following manner. In the streaming phase, most of the bubbles rise together in the stream and have high rise velocities of nearly equal value, while a few bubbles located at the edge of the stream and in the liquid away from the stream have much lower rise velocities and in some cases even negative rise velocities.
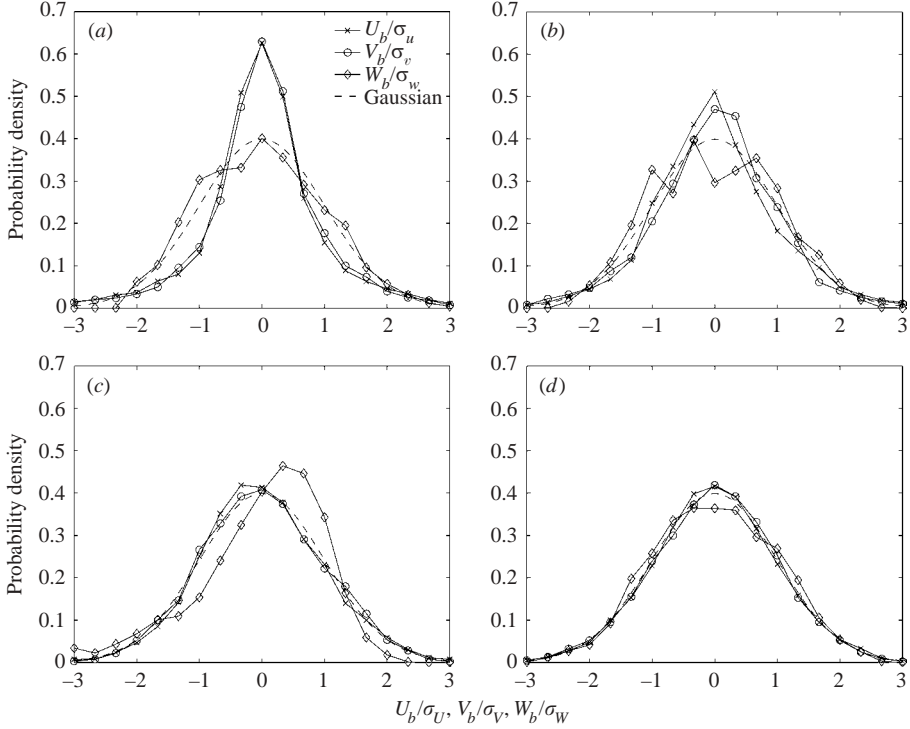
FIGURE 21. Probability density functions of the bubble velocities for the ellipsoidal bubbles: (a) $\alpha = 2\%$, (b) $\alpha = 6\%$, non-streaming phase $(t(g/d)^{1/2} \in [25, 90])$, (c) $\alpha = 6\%$, streaming phase $(t(g/d)^{1/2} \in [100, 180])$, (d) $\alpha = 12\%$. $Eo = 5$. The mean velocity is set to zero and the velocities are scaled by their standard deviations, σ_U, σ_V, and σ_W, and $[-3\sigma, +3\sigma]$ is discretized into 19 intervals. 500 equidistant time samples in $[T_i, T_f]$ are used to determine (a) and (d). 200 equidistant time samples are used in $[25, 90]$ and $[100, 180]$ to determine (b) and (c).

The diffusion of fluid particles in turbulent flows was studied by Taylor (1921), who proved that the mean square displacement of the fluid particles increases at a uniform rate at large times. When this result is transposed to the problem of following the motion of bubbles instead of fluid particles, it can be written, in our notations and in the case of the vertical direction component, as $X_b^2(T \mid T_0) = 2\langle W_b'\rangle^2 T_L(T - T_0)$ for $(T - T_0) \gg T_L$, where $T_L = \int_0^\infty R_{WW}(T)\,dT$ is the Lagrangian integral time scale and $R_{WW}(T)$ is the Lagrangian autocorrelation function of the velocity fluctuations of the bubbles, which is defined later in this section. An alternative method to test the validity of a diffusion model is therefore to verify whether the pseudodispersion coefficients, defined by $D'(T) = X_b^2(T \mid T_0)/2(T - T_0)$, converge as $T - T_0$ increases. Here, $D'(T)$ stands for the pseudodispersion coefficient in any of the three spatial coordinates, $D_x'(T)$, $D_y'(T)$ or $D_z'(T)$. It is computed by averaging over the $[T_i, T_f]$ interval defined in table 1 in order to avoid the initial transient, using a discretized form of the integral:

$$D'(T) = \frac{1}{T_f - T_i - T} \int_{T_i}^{T_f - T} \frac{X_b^2(T \mid T_0)}{2(T - T_0)}\,dT_0, \qquad (4.5)$$

T ranging from 0 to $T_f - T_i$. The time-averaging over $T_0 = [T_i, T_f]$ is a substitute for ensemble-averaging over a large number of simulations with different initial
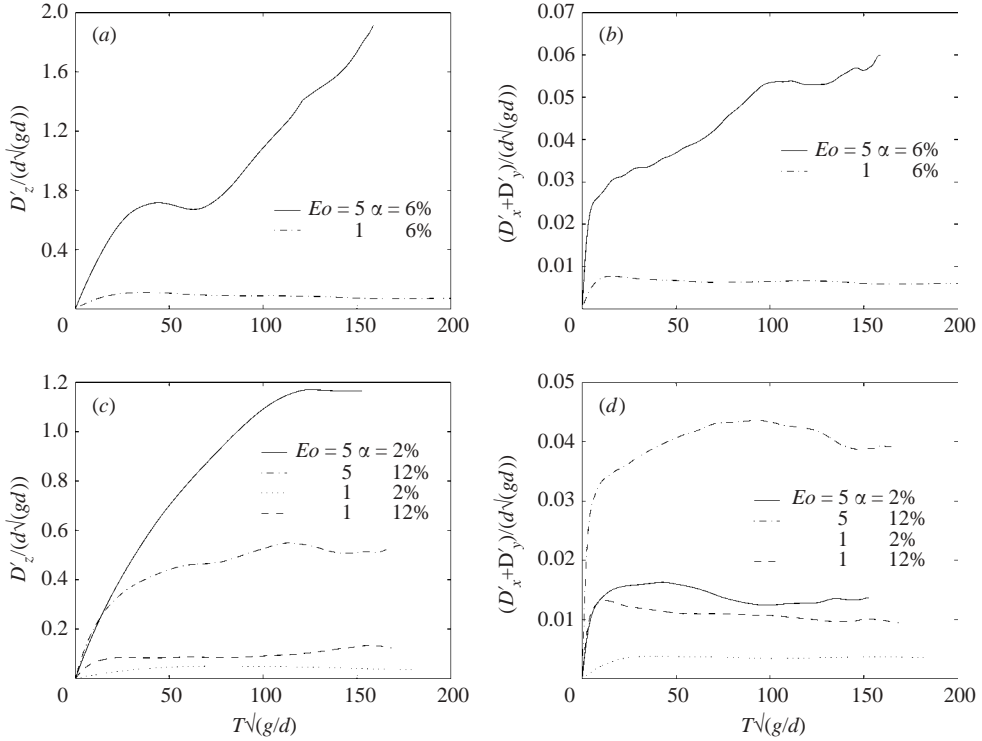
FIGURE 22. Dispersion coefficients versus time: (*a*) vertical and (*b*) horizontal coefficients for $\alpha = 6\%$, (*c*) vertical and (*d*) horizontal coefficients for $\alpha = 2\%$ and 12%.

conditions, which is not feasible. It leads to lower statistical variability than if $D'(T)$ is calculated using a single value of T_0. Nevertheless, while the grid independence tests show that the motion of the bubbles is well resolved, it will be shown that the results are likely to be affected by the relatively small number of bubbles and the limited simulation time. In spite of that, the results provide important qualitative insight into the dispersion process of the bubbles for different void fractions and different levels of bubble deformation.

Since the x and y directions are equivalent, $D'_x(T)$ and $D'_y(T)$ are approximately equal. $D'_x(T) + D'_y(T)$ and $D'_z(T)$ are non-dimensionalized by $d(gd)^{1/2}$ and are shown in figure 22. For $Eo = 5$ and $\alpha = 6\%$, neither $D'_x(T) + D'_y(T)$ nor $D'_z(T)$ show any sign of converging as T increases. This is consistent with the strong asymmetry noted previously in the probability density of W_b and suggests that the dispersion process in the streaming phase cannot be considered Gaussian. However, we note that a definitive answer awaits further simulations past the time when we had to stop this run. For all other cases, $D'_x(T) + D'_y(T)$ and $D'_z(T)$ seem to converge as T grows. For $Eo = 5$, convergence is slower for $\alpha = 2\%$ than for $\alpha = 12\%$, which is consistent with the larger non-Gaussian effects seen in figure 21(*a*) than in figure 21(*d*). The limits of $D'_x(T) + D'_y(T)$ and $D'_z(T)$ as T increases are the dispersion coefficients $D'_x + D'_y$ and D'_z. We then define the horizontal and vertical Lagrangian integral time scales of the bubble' motion, T_{x+y} and T_z, by $D'_x + D'_y = \langle (U_b'^2 + V_b'^2)^{1/2} \rangle^2 T_{x+y}$ and $D'_z = \langle W_b'^2 \rangle^2 T_z$, respectively.

The dispersion coefficients are much larger for $Eo = 5$ than for $Eo = 1$. For example, for $\alpha = 2\%$, D'_z is approximately 30 times larger for $Eo = 5$ than for $Eo = 1$. Since W_b'
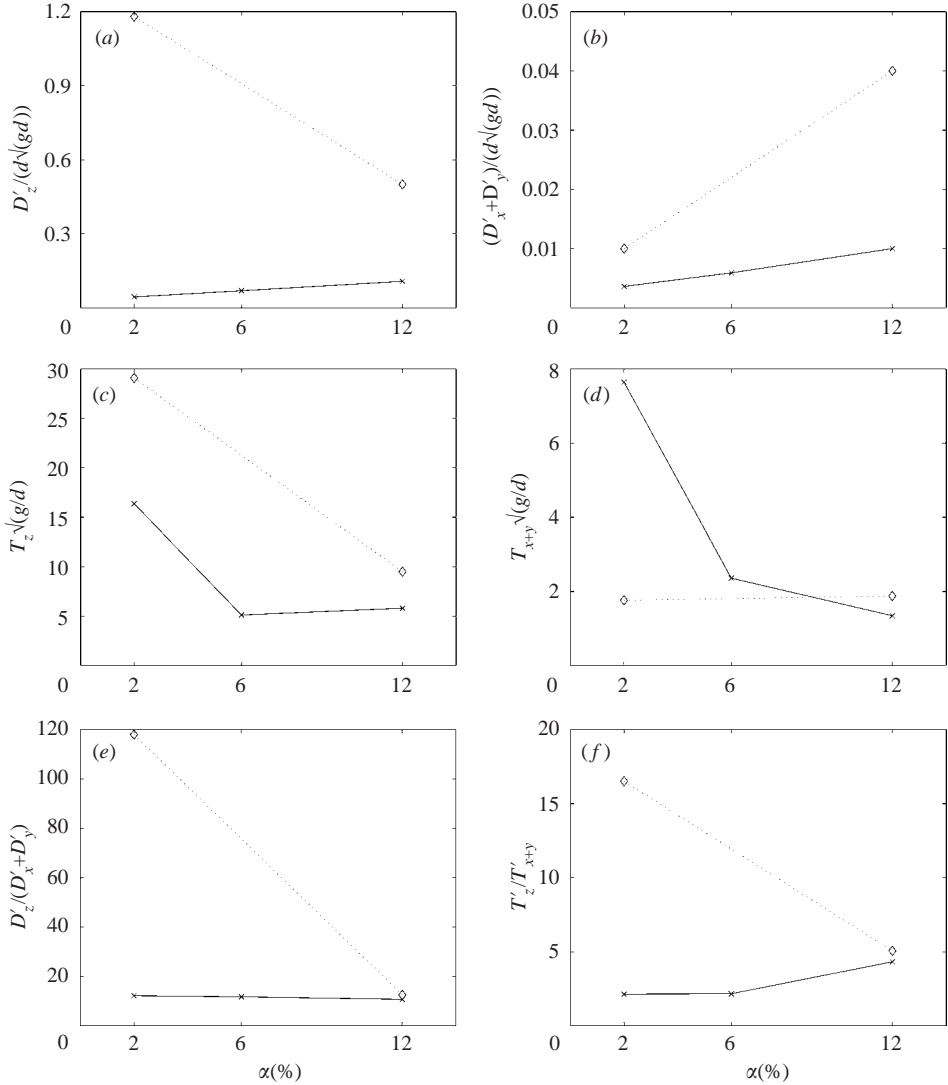
FIGURE 23. (*a*) Vertical and (*b*) horizontal diffusion coefficients. (*c*) Vertical and (*d*) horizontal Lagrangian time scales. Ratio of the vertical and horizontal (*e*) diffusion coefficients and (*f*) Lagrangian time scales. The values for $Eo = 5$, $\alpha = 6\%$ could not be determined owing to the transition to the streaming mode. T_z and T_{x+y} are defined by $D'_z = \langle W'_b \rangle^2 T_z$ and $D'_x + D'_y = \langle (U'^2_b + V'^2_b)^{1/2} \rangle^2 T_{x+y}$. $\diamond$, $Eo = 1$; $\times$, 1.

is 3.9 times larger for $Eo = 5$ than for $Eo = 1$, the Lagrangian integral time scale T_z is about two times larger for $Eo = 5$ than for $Eo = 1$. The ratio of the values of D'_z for $Eo = 5$ and $Eo = 1$ decreases with the void fraction, though. At $\alpha = 12\%$, it is only 4. The ratio of values of $D'_x + D'_y$ for $Eo = 5$ and $Eo = 1$ is also equal to 4, at $\alpha = 2\%$ and $\alpha = 12\%$.

The diffusion coefficients and Lagrangian integral time scales are shown versus α in figure 23. The diffusion coefficients generally increase with the void fraction, like the velocity fluctuations, with the exception of D'_z for $Eo = 5$, which is smaller at $\alpha = 12\%$ than at $\alpha = 2\%$ by a factor of two. The Lagrangian integral time scales generally
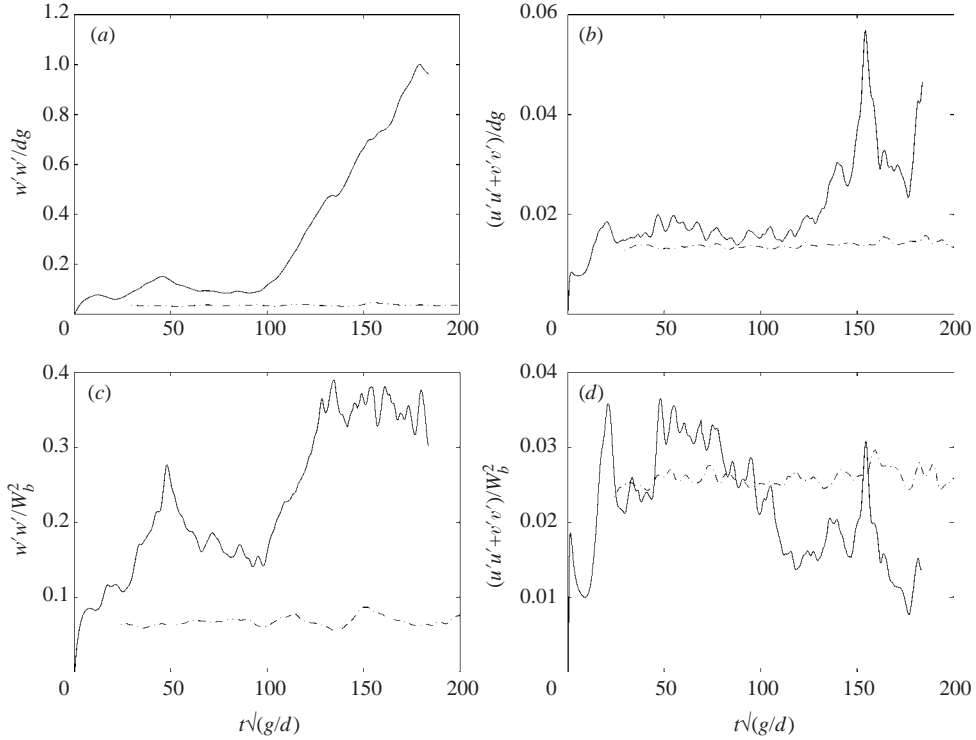
FIGURE 24. (*a*) Vertical and (*b*) horizontal Reynolds stresses scaled by dg versus time for $\alpha = 6\%$. (*c*) Vertical and (*d*) horizontal Reynolds stresses scaled by the instantaneous barycentre rise velocity $W_b(t)$. The data for $Eo = 1$ before $t(g/d)^{1/2} = 30$ is missing. —, $Eo = 5$; –·–, 1.

decrease when α increases. The anisotropy of both the diffusion coefficients and the Lagrangian integral time scales is very high, particularly for $Eo = 5$, $\alpha = 2\%$. Bunner & Tryggvason (2002*a*) showed that the number of bubbles in the periodic cell, N_b, has a strong effect on the horizontal components of these two quantities in the case of spherical bubbles. For example, $D'_x + D'_y$ is more than twice as large for $N_b = 216$ as it is for $N_b = 27$. Although no study of the effect of system size was conducted for deformable bubbles, we expect this effect to be significant for ellipsoidal bubbles too, in particular for $D'_x + D'_y$ and T_{x+y}. Larger simulations are clearly needed to obtain results that do not depend on the size of the computational domain, especially for the horizontal components.

4.5. *Liquid velocity fluctuations*

Although the Reynolds number of the simulations reported here is low and the flow field around a bubble remains laminar, averaging approaches used to model two-phase flows lead to the appearance of pseudoturbulent Reynolds stresses characterizing the randomly fluctuating liquid velocity produced by the motion of the bubbles. $w'w'$ and $u'u' + v'v'$ are shown versus time in figure 24(*a*, *b*) for $\alpha = 6\%$. The off-diagonal Reynolds stresses, $\langle u'v' \rangle$, $\langle u'w' \rangle$ and $\langle v'w' \rangle$, are approximately zero but not exactly zero because of the limited system size. For $Eo = 5$ and $\alpha = 6\%$, both $w'w'$ and $u'u' + v'v'$ increase when the deformable bubbles form a stream. However, $(u'u' + v'v')/W_b^2$ is lower in the streaming phase than in the non-streaming phase, whereas $w'w'/W_b^2$ is larger in the streaming phase than in the non-streaming phase. The Reynolds
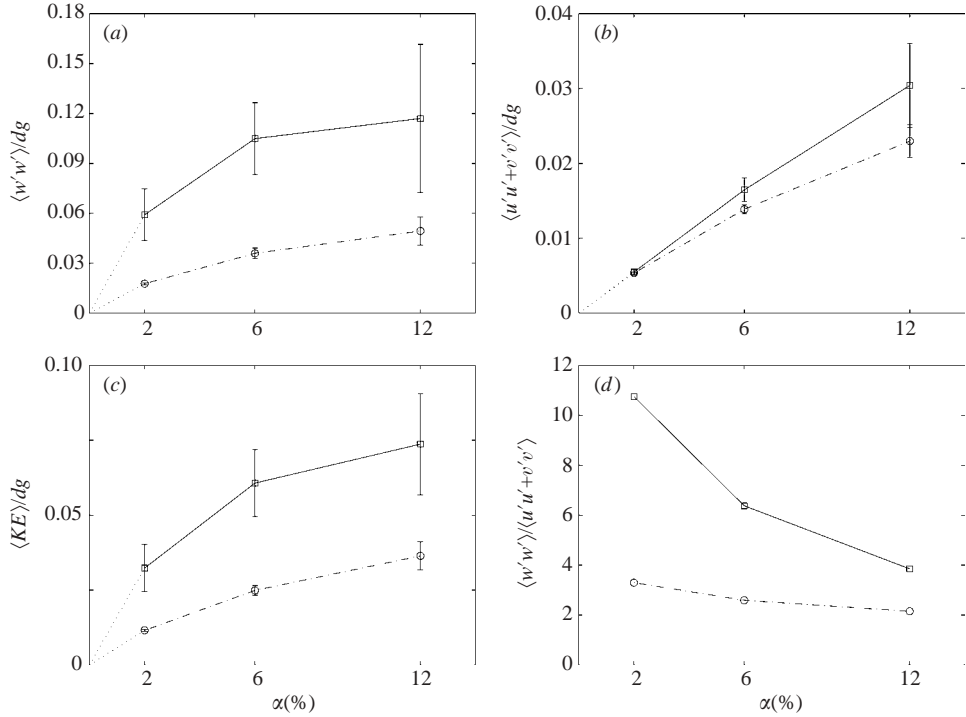
FIGURE 25. The time-averaged Reynolds stresses and pseudoturbulent kinetic energy $\langle KE \rangle$ as a function of α for $\square$, $Eo = 5$ and $\bigcirc$, $Eo = 1$: (a) Vertical Reynolds stress, (b) horizontal Reynolds stress, (c) pseudoturbulent kinetic energy. (d) Ratio of the vertical over horizontal Reynolds stresses. The points for $Eo = 5$, $\alpha = 6\%$ correspond to the averages of the data in the [25, 90] time interval, before the streaming phase.

stresses induced by the bubbles in the liquid are larger for $Eo = 5$ than for $Eo = 1$. Stewart (1995) showed that the wake capture and collision process of deformable bubbles implied a large amplification of turbulent kinetic energy production. A more detailed examination of the wake structure by Brücker (1999b) suggested that this amplification is due to the enlargement of the wake during the collision. While these observations are derived from experiments with bubbles of larger deformation and rise velocity, they are more consistent with the larger Reynolds stresses seen for $Eo = 5$, where events of wake capture and collision occur frequently, than for $Eo = 1$, where no such event has been observed.

The average Reynolds stresses and the pseudoturbulent kinetic energy are shown versus α in figure 25. Like the bubble velocity fluctuations, the horizontal component of the liquid velocity fluctuations grows faster with α than the vertical component. The anisotropy of the Reynolds stress tensor therefore decreases as α increases, as seen in figure 25(d). We note that this anisotropy is much larger for deformable bubbles than for spherical bubbles.

An estimate of the time-averaged Reynolds stresses can be obtained for spherical bubbles using potential flow theory (Biesheuvel & van Wijngaarden 1984):

$$\langle u'_i u'_j \rangle = \begin{pmatrix} \frac{3}{20} & 0 & 0 \\ 0 & \frac{3}{20} & 0 \\ 0 & 0 & \frac{4}{20} \end{pmatrix} \alpha \langle W_b \rangle^2. \tag{4.6}$$
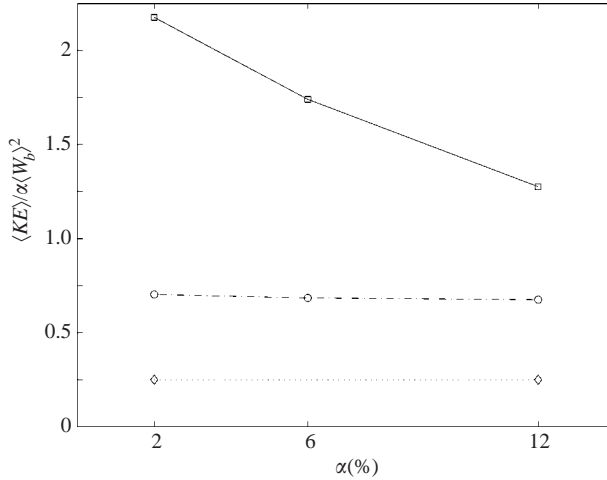
FIGURE 26. Pseudoturbulent kinetic energy $\langle KE \rangle$ scaled by $\alpha \langle W_b \rangle^2$. The point for $Eo = 5$, $\alpha = 6\%$ corresponds to the average of the data in the $[25, 90]$ time interval, before the streaming phase. $\square$, $Eo = 5$; $\circ$, 1; $\diamond$, potential flow.

The pseudoturbulent kinetic energy scaled by $\alpha \langle W_b \rangle^2$ is shown versus α in figure 26. As noted by Bunner & Tryggvason (2002b), $\alpha \langle W_b \rangle^2$ provides a good scaling for $\langle KE \rangle$ in the case of spherical bubbles, even though the values of $\langle KE \rangle/(\alpha \langle W_b \rangle^2)$ for the potential flow model and the simulation results differ considerably. For deformable bubbles, however, this scaling is clearly not applicable.

To examine the structure of the velocity field, we determine the isotropic kinetic spectrum, $E(k)$. The spectrum is computed from the velocity and density fields $\boldsymbol{u}$ and ρ in the entire computational domain Ω and is normalized such that:

$$\sum_k E(k) \Delta k = \frac{1}{2} \int_\Omega \rho \|\boldsymbol{u}\|^2 \, \mathrm{d}V. \tag{4.7}$$

First, the discrete Fourier transforms of the velocities multiplied by the square root of the density are calculated. Then, the energy content is summed in spherical shells of width Δk centred at $k = (k_x^2 + k_y^2 + k_z^2)^{1/2}$, where (k_x, k_y, k_z) is the wave vector. The kinetic energy spectrum is shown at four consecutive times for $Eo = 5$, $\alpha = 2\%$ in figure 27(a), for $Eo = 5$, $\alpha = 6\%$ in figure 27(b), and for $Eo = 5$, $\alpha = 12\%$ in figure 27(d). Since the flow field is initially quiescent and no external forcing is applied, the long waves contain little energy immediately after the bubbles are released. The peaks at $kd = 2.10$, 3.04 and 3.85 at the first times in figures 27 (a), (b) and (d) correspond to the average horizontal or vertical distances between neighbouring bubbles in the perturbed array. As pointed out by Esmaeeli & Tryggvason (1996), the bubbles can be viewed as a stirring force acting on the liquid. As time increases, energy is fed by the bubbles into the long wave components of the spectrum, while the energy content of the short-wave components of the spectrum remains approximately constant. Unlike the two-dimensional results of Esmaeeli & Tryggvason (1996), here there exists a statistical steady state, where the production of energy by the bubbles balances the dissipation of energy in the liquid and at the bubble interface. The exception is the $\alpha = 6\%$ case, in figure 27(b), where the increase in the pseudoturbulent kinetic energy due to streaming leads to an increase of $E(k)$ at all wavenumbers k, but particularly at low k, which reflects the formation of a large-scale flow structure. At $\alpha = 2\%$, $E(k)$
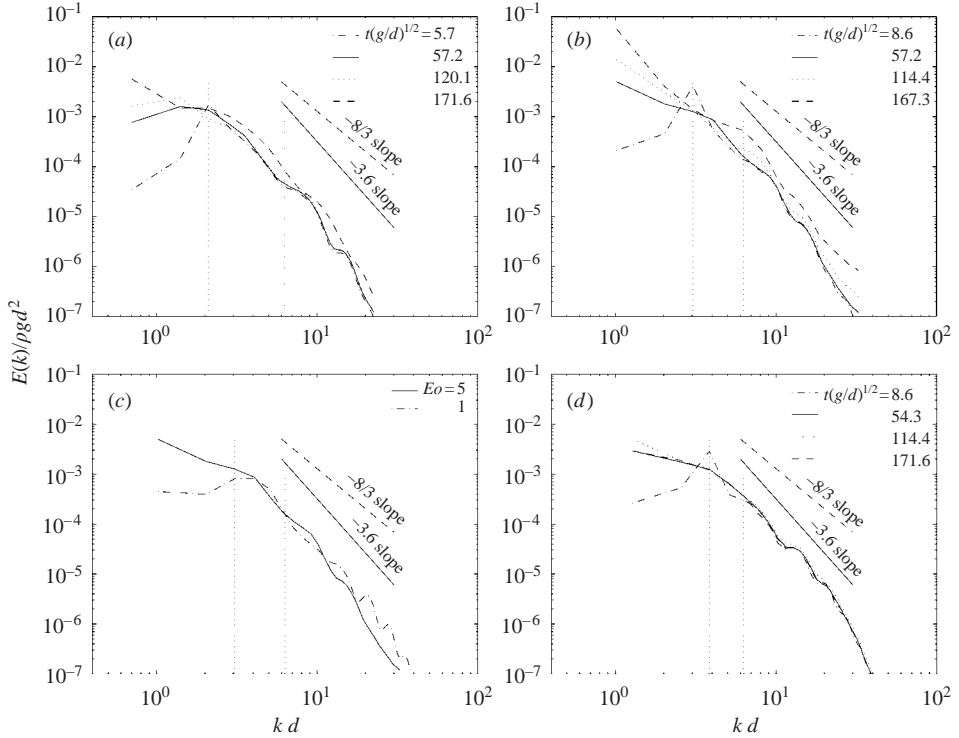
FIGURE 27. Kinetic energy spectrum for (a) $Eo = 5$, $\alpha = 2\%$, (b) $Eo = 5$, $\alpha = 6\%$, (c) $Eo = 5$ and $Eo = 1$, $\alpha = 6\%$, $t(g/d)^{1/2} = 57.2$, (d) $Eo = 5$, $\alpha = 12\%$. The vertical dotted lines correspond to the mean spacings between the bubbles' centroids, which are, respectively, $kd = 2.10$, 3.04 and 3.85 for $\alpha = 2$, 6 and 12%, and to the bubble diameter, $kd = 6.28$.

at low k increases also steadily and monotonically with time, which is consistent with the increase in $w'w'$ seen at later times for $Eo = 5$, $\alpha = 2\%$, but does not reflect a transition to streaming.

A comparison of the kinetic energy spectrum for the spherical and the deformable bubbles at $\alpha = 6\%$ in figure 27(c) reveals that the spectra are similar at high wavenumbers. The larger kinetic energy seen in figure 25(c) for $Eo = 5$ than for $Eo = 1$ manifests itself mainly in the larger energy content of the long wavelengths. It appears that the kinetic energy spectrum can be separated into two regions, low and high wavenumbers. In the low-wavenumber region, the spectrum is determined by the interaction between the bubbles and the collective structures that they form. Since these structures were shown to be qualitatively different, it is reasonable to see differences in spectrum at low wavenumbers. In the high-wavenumber region, the spectrum corresponds to velocity fluctuations on length scales smaller than the bubble diameter and is therefore determined primarily by the structure of the flow around individual bubbles, particularly in the wake. While stronger vorticity is generated at the interface of the deformable bubbles than at the interface of spherical bubbles, which should result in stronger velocity fluctuations in the wake, the structure of the flow around the bubbles is the same, which is consistent with the observation that the spectra at high wavenumbers are approximately the same.

To our knowledge, the only other study of liquid velocity fluctuations induced by bubbles in homogeneous bubbly flows is the experimental work of Lance &

α (%)	Eo	$\langle Re_b \rangle$	$\langle w'w' \rangle/gd$ (10^{-2})	$\langle u'u' + v'v' \rangle/gd$ (10^{-2})	$\epsilon_f/\rho_f(g^3 d)^{1/2}$ (10^{-2})	l_K/d	u_K/W_b	λ/d	Re_λ
2	1	27.14	1.77	0.54	1.61	0.219	0.168	0.692	1.29
2	5	25.84	5.93	0.55	1.54	0.221	0.175	0.836	3.68
6	1	23.35	3.59	1.39	4.14	0.173	0.248	0.448	1.76
6	5	22.87	10.5	1.65	3.92	0.175	0.249	0.718	4.33
12	1	20.09	4.98	2.30	7.07	0.151	0.329	0.414	1.94
12	5	20.82	11.7	3.04	6.59	0.154	0.312	0.611	4.06

TABLE 2. Properties of the velocity fluctuations in the liquid: vertical and horizontal Reynolds stresses $\langle w'w' \rangle$ and $\langle u'u' + v'v' \rangle$, dissipation rate per unit volume, ϵ_f, Kolgomorov length and velocity scales l_K and u_K, Taylor miscroscale λ, microscale Reynolds number Re_λ. ϵ_f is the total dissipation rate in the liquid, $\epsilon_f = \sum \epsilon_{f_{ij}}$, where $\epsilon_{f_{ij}} = (1/\Omega_f) \int_{\Omega_f} \mu (\partial u_i/\partial x_j + \partial u_j/\partial x_i)^2 \, dV$. The Kolmogorov scales are determined according to $l_K = (\nu_f^3 \rho_f/\epsilon_f)^{1/4}$ and $u_K = (\epsilon_f \nu_f/\rho_f)^{1/4}$. λ is evaluated roughly by using the single-phase formula for homogeneous isotropic turbulence, $\epsilon_f = 15 \nu_f u'^2/\lambda^2$, where u' is the r.m.s velocity determined from the pseudoturbulent kinetic energy in the liquid, $u' = (2 \langle KE \rangle/3)^{1/2}$ (Tennekes & Lumley 1972). Re_λ is defined as $Re_\lambda = u'\lambda/\nu_f$. The mean rise Reynolds number of the bubbles, $\langle Re_b \rangle$, is added for reference.

Bataille (1991), who found that the kinetic energy spectrum follows a power law with a slope of $-8/3$ at high wavenumbers. Our results show that a power law with a slope of approximately -3.6 applies at all void fractions for both spherical and deformable bubbles. The difference in the slopes can be attributed to the difference in the Reynolds number between the experiments of Lance & Bataille (1991), where it is of order 1000, and our simulations, where it is of order 20. In addition, the values of the slope in the simulation results is quite imprecise because of the limited range of wavenumbers due to the small size of the computational domain and because of the disturbance created by the jump in density and velocity at the interface, whose effect on the spectrum is difficult to evaluate. Given these limitations, the value of the results shown in figure 27 is mainly in the qualitative information provided by comparisons between the different cases.

The main statistical quantities of the pseudoturbulence in the liquid are summarized in table 2. Since the ellipsoidal and spherical bubbles have approximately the same rise velocity, the steady-state dissipation rates, and hence the Kolmogorov microscales, are also approximately equal. However, owing to the larger pseudoturbulence induced in the liquid by the ellipsoidal bubbles, the Taylor microscale and the microscale Reynolds number are larger for $Eo = 5$ than for $Eo = 1$.

4.6. *Effect of initial conditions*

For the deformable bubbles, streaming is only observed in the $\alpha = 6\%$ simulation. At $\alpha = 12\%$, the formation of a stream seems to be inhibited by the high void fraction. One possible explanation is that the large velocity fluctuations induced in the liquid by the bubbles disturb the vertical arrangement of the bubbles. A simpler explanation is that the bubbles do not have enough space to arrange themselves into streams. At $\alpha = 2\%$, it is possible that the bubbles will form a stream if the simulation were pursued until a later time. However, we have not been able to establish a criterion to determine under which conditions the streaming instability appears. As a preliminary study, and also to confirm our belief that bubbles at $\alpha = 2\%$ can form a stream, we have performed two simulations with 27 bubbles, $Eo = 5$, and $\alpha = 2\%$, in which the bubbles are initially located in a vertical column. The same numerical resolution was
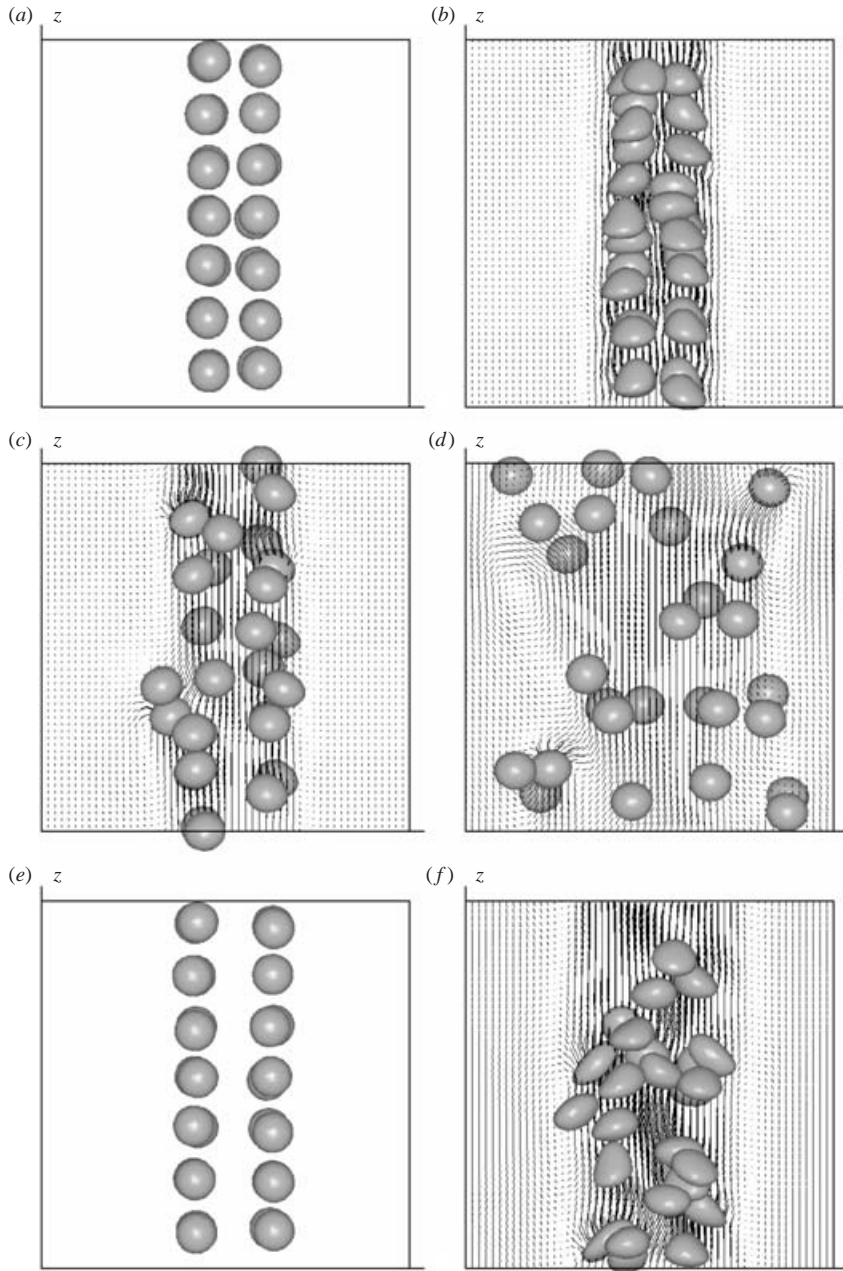
FIGURE 28. (*a*) Initial configuration for cases A ($Eo = 5$) and B ($Eo = 1$). (*b*) Case A at $t(g/d)^{1/2} = 5.72$. (*c*) Case B at $t(g/d)^{1/2} = 5.72$. (*d*) Case B at $t(g/d)^{1/2} = 14.31$. (*e*) Initial configuration for case C ($Eo = 5$). (*f*) Case C at $t(g/d)^{1/2} = 14.31$. The streamlines in a plane vertical cross-section are added. No streamlines are shown in (*a*) and (*e*) because the velocity field is equal to zero at $t = 0$.

used as in the $Eo = 5$, $\alpha = 2\%$ simulation given in table 1. For the first case, denoted case A, the configurations of the 27 bubbles at $t = 0$ and $t(g/d)^{1/2} = 5.72$ are shown in figures 28(*a*) and 28(*b*). For the second case, denoted case C, the configurations of the 27 bubbles at $t = 0$ and $t(g/d)^{1/2} = 14.31$ are shown in figures 28(*e*) and 28(*f*). To
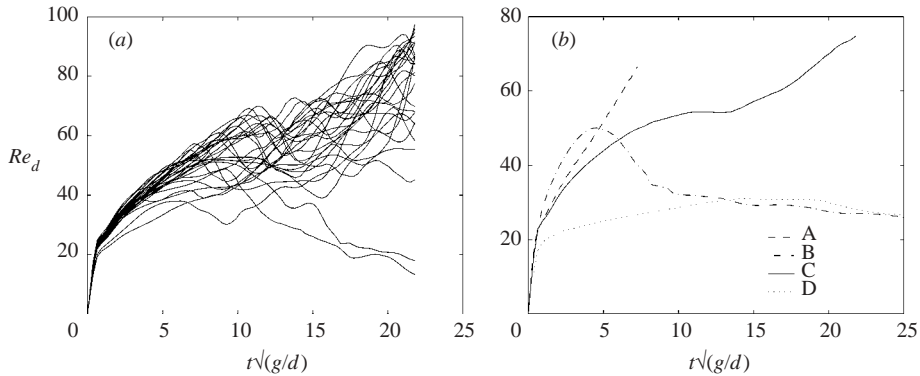
FIGURE 29. (*a*) Drift Reynolds number of the 27 bubbles for case C ($Eo = 5$) versus time. (*b*) Average drift Reynolds number of cases A ($Eo = 5$), B ($Eo = 1$), C ($Eo = 5$) and D ($Eo = 5$) versus time.

highlight the difference between spherical and ellipsoidal bubbles, a third simulation, denoted case B, was performed with 27 bubbles, $Eo = 1$, $\alpha = 2\%$, and the initial configuration shown in figure 28(*a*). The configuration of the 27 spherical bubbles is shown at $t(g/d)^{1/2} = 5.72$ in figure 28(*c*) and at $t(g/d)^{1/2} = 14.31$ in figure 28(*d*).

The average drift velocities of cases A, B and C are shown in figure 29(*b*), along with the corresponding values for the $Eo = 5$, $\alpha = 2\%$ simulation already reported in §4.2, which is denoted case D. The following observations can be made from the results. The deformable bubbles in cases A and C form a stream and their rise velocities increase steadily. The rise velocity in case A increases faster than the rise velocity in case C because the bubbles are initially located closer to each other. Both simulations A and C were stopped when the drift Reynolds number reached about 70, because of the insufficient numerical resolution mentioned in §4.1. In case C, most bubbles remain in the stream until the end of the simulation, with the exception of two bubbles, which escape the stream and move into the region of the flow field dominated by the liquid. Since the net momentum flux through the boundaries of the computational domain is zero (§§2 and 3), the liquid away from the stream experiences a downflow. As a result, these two bubbles decelerate and their drift Reynolds number drops below the average drift Reynolds number of case D, 25.34, as seen in figure 29(*a*). In contrast, the vertical column of spherical bubbles (case B) breaks up almost immediately, as seen in figures 28(*c*) and 28(*d*). The drift Reynolds number of case B rises briefly to a value of about 50. However, as the spherical bubbles disperse through the computational domain, Re_d decreases and tends towards the same value as in the case where the bubbles are initially in a perturbed regular array, 26.60.

To summarize, the results of these simulations suggest that streaming will occur for deformable bubbles at $\alpha = 2\%$ too and show that the initial conditions have a strong effect on when streaming is initiated. While limitations in computational resources prevented us from exploring a wider range of parameters, we would like to discuss the issue of streaming further and raise a number of questions that remain unanswered and could be topics of future study. (i) What is the range of void fractions at which streaming can occur? This paper has shown that streaming can occur at $\alpha = 2\%$ and $\alpha = 6\%$. At higher void fractions, it is possible that the presence of large concentrations of bubbles prevents the formation of a stream. At very low void

fractions, bubbles do not interact with each other and are therefore unlikely to form a stream. (ii) When is streaming initiated? Since interactions between bubbles are more frequent when the void fraction is larger, it is likely that streaming will be initiated earlier at larger void fractions. This is consistent with the fact that streaming was observed at $t(g/d)^{1/2} \approx 100$ for $\alpha = 6\%$ (figure 2) but was not observed for $\alpha = 2\%$ (figure 12), even though the simulation was carried on until $t(g/d)^{1/2} \approx 200$. The initiation time likely also depends on the number of bubbles in the numerical simulation or experimental set-up. For example, if a large number of simulations with different initial conditions were carried out for $N_b = 27$ and 216, it is likely that the streaming would, on average, start earlier for $N_b = 216$ than for $N_b = 27$, because of the larger number of bubble pairs. (iii) Once the stream has formed, is it a permanent feature or can it break up? We observed in figures 2(a) and 29(a) that some bubbles moved away from the stream. If the void fraction is very low and the bubbles disperse too widely to be recaptured, a possible scenario could be that the stream disappears, as Stewart (1995) sometimes observed in experiments. (iv) What are the limiting values of the rise velocity, Reynolds stresses and other quantities? (v) What is the threshold value of Eo, below which streaming is unlikely to occur? Given the mechanism illustrated in figure 4, it is likely to correspond to the value for which the lift force changes direction as the deformation of the bubble increases (Ervin & Tryggvason 1997).

Stewart (1995) examined the interaction of bubbles experimentally, for bubbles with slightly larger deformations, $Eo > 6.0$, and Reynolds numbers, $Re_b > 100$, than in our simulations. He observed that the interaction of two bubbles is characterized by wake capture followed by collisions. For multiple bubbles, this leads to the formation of clusters, where bubbles leapfrog each other, in a repeated process of wake capture and collision similar to what is depicted in figure 15. Although we were not able to pursue the simulations for a long time after initiation of streaming, animations of the results for $Eo = 5$ and $\alpha = 2\%$ (results of §4.6) and 6% (results of §4.1) clearly showed occurrences of this leapfrogging process. Stewart noted that the process is discontinuous if the cluster contains only a small number of bubbles and becomes approximately continuous if the cluster involves more than about 10 bubbles, in which case he called the structure formed by the bubbles a 'chimney.' Additional complications arise in the experiments because of breakup and coalescence of the bubbles, but is appears that these chimneys are essentially the same phenomenon as the streams observed in our simulations.

The results of §4.6 strongly suggest that the bubbles shown in §§4.2, 4.4 and 4.5 for $Eo = 5$ and $\alpha = 2\%$ will eventually form a stream as they do for the $Eo = 5$, $\alpha = 6\%$ case. The results shown in these sections, where the bubbles are relatively uniformly distributed, might therefore not apply to large bubble columns where the bubbles have transitioned into streams. Since transition to streaming apparently does not take place instantaneously the results would, however, apply to the bubbles in the region where they formed, such as near injectors or below plunging waves.

5. Conclusion

The motion of buoyant deformable bubbles in a homogeneous flow is studied by direct numerical simulations, where the effects of viscosity, inertia, interface deformation and surface tension are all accounted for. The results are compared with the corresponding results for spherical bubbles. The rise Reynolds number is 17–26, depending on the void fraction, which ranges between 2% and 12%. The

α (%)	Eo	$\langle Re_d\rangle$	$\langle Re_b\rangle$	$\dfrac{\langle W'_b\rangle}{\langle W_b\rangle}$	$\dfrac{\langle(U'^{2}_b+V'^{2}_b)^{1/2}\rangle^{1/2}}{\langle W'_b\rangle}$	$\dfrac{D'_z}{a\langle W_b\rangle}$	$\dfrac{(D'_x+D'_y)}{a\langle W_b\rangle}$	$\dfrac{T_z\langle W_b\rangle}{a}$	$\dfrac{T_{x+y}\langle W_b\rangle}{a}$
2	1	26.60	27.14	0.0573	0.0240	0.0973	0.0080	29.6	13.8
2	5	25.34	25.84	0.2337	0.0874	2.7380	0.0232	50.2	3.04
6	1	21.95	23.35	0.1493	0.0683	0.1775	0.0152	7.95	3.25
6	5	21.50	22.87	0.3147	0.1583	–	–	–	–
12	1	17.68	20.09	0.2027	0.1273	0.3195	0.2990	9.61	1.84
12	5	18.32	20.82	0.3306	0.2104	1.4410	0.1153	13.2	2.60

TABLE 3. Transport properties of the bubbles. For $Eo=5$, $\alpha=2\%$ and $Eo=5$, $\alpha=6\%$, the results are for the phase before streaming and are therefore not expected to be the steady-state results. They are given to provide a quick summary of the results. For $Eo=5$, $\alpha=6\%$, it was not possible to determine the diffusion coefficients and Lagrangian integral time scales beause of the short amount of time before formation of the stream. For $Eo=5$, $\alpha=2\%$, the amount of simulation time was sufficient for these quantities to be determined. a is the bubble radius.

aspect ratio of the deformable bubbles is approximately 1.4. The simulations were performed in a periodic cell including 27 bubbles. The main statistical results are summarized in table 3. The major observations and conclusions are as follows.

(i) An analysis of the microstructure of the bubble distribution reveals a preference for pairs of deformable bubbles to be aligned vertically and for pairs of spherical bubbles to be aligned horizontally. The dynamic interaction process of two bubbles is dominated by wake effects. A bubble moving in the wake of another bubble is attracted toward the leading bubble. Because larger amounts of vorticity are generated at the interface of deformable bubbles, the wake effect is stronger for deformable bubbles than for spherical bubbles. As a result, two deformable bubbles usually collide and then rotate about each other, whereas two spherical bubbles usually do not collide. After rotation, when the two bubbles are aligned side-by-side, they repel.

(ii) For $\alpha=2\%$ and 6%, the stronger wake effect for deformable bubbles leads to the formation of large-scale flow structures, where the bubbles gather into vertical columns, which we call streams. While we were not able to determine the final steady-state properties of the flow after the bubbles form a stream, we did observe a marked increase in the velocity of the bubbles and the velocity fluctuations of the bubbles and the liquid. In contrast, spherical bubbles remain distributed throughout the flow field and their motion remains statistically steady. The difference between the behaviour of the spherical and deformable bubbles can be explained by considering the lift force acting on a bubble moving in the wake of another bubble. For spherical bubbles, the lift force points out of the wake, so that the bubble moves out of the wake. For deformable bubbles, the lift force points toward the wake, so that the bubble moves toward the wake, thus reinforcing the stream.

(iii) The deformable bubbles experience much stronger interactions than the spherical bubbles, and they therefore induce much larger velocity fluctuations in the liquid. An analysis of the kinetic energy spectra shows that the difference lies mainly in a larger energy content at wavelengths larger than the bubble diameter, indicating an inverse energy cascade, where energy is transferred from small scales to large scales.

(iv) The self-dispersion process of the bubbles can roughly be characterized as Gaussian when the bubbles are not streaming. The vertical velocity fluctuations and diffusion coefficients of the bubbles are much larger than their horizontal counterparts. The anisotropy decreases as the void fraction increases.

REFERENCES

BATCHELOR, G. K. 1967 *An Introduction to Fluid Dynamics.* Cambridge University Press.

BATCHELOR, G. K. & TOWNSEND, A. A. 1956 Turbulent diffusion. *Surveys in Mechanics.* Cambridge University Press.

BIESHEUVEL, A. & WIJNGAARDEN, L. VAN 1982 The motion of pairs of gas bubbles in a perfect fluid. *J. Engng Maths.* **16**, 349–365.

BIESHEUVEL, A. & WIJNGARDEN, L. VAN 1984 Two-phase flow equations for a dilute dispersion of gas bubbles in liquid. *J. Fluid Mech.* **148**, 301–318.

BLANCO, A. & MAGNAUDET, J. 1995 The structure of the axisymmetric high-Reynolds number flow around an ellipsoidal bubble of fixed shape. *Phys. Fluids* **7**, 1265–1274.

BOSSIS, G. & BRADY, J. F. 1984 Dymanic simulations of sheared suspensions. I. General method. *J. Chem. Phys.* **80**, 5141–5154.

BRÜCKER, C. 1999*a* A detailed study of the role of the wake on the motion of single bubbles and bubble pairs using an advanced PIV-method. *Proc. 9th Workshop on Two-Phase Flow Predictions,* IVT MLU Halle-Wittenberg.

BRÜCKER, C. 1999*b* Structure and dynamics of the wake of bubbles and its relevance for bubble interaction. *Phys. Fluids* **11**, 1781–1796.

BUNNER, B. & TRYGGVASON, G. 1999*a* Direct numerical simulation of three-dimensional bubbly flows. *Phys. Fluids* **11**, 1167–1169.

BUNNER, B. & TRYGGVASON, G. 1999*b* An examination of the flow induced by the motion of many buoyant bubbles. *J. Visualiz.* **2**, 153–158.

BUNNER, B. & TRYGGVASON, G. 2002*a* Dynamics of homogeneous bubbly flows. Part 1. Rise velocity and microstructure of the bubbles. *J. Fluid Mech.* **466**, 17–52.

BUNNER, B. & TRYGGVASON, G. 2002*b* Dynamics of homogeneous bubbly flows. Part 2: Velocity fluctuations. *J. Fluid Mech.* **466**, 53–84.

CHAHINE, G. L. 1994 Strong interactions bubble/bubble and bubble/flow. In *IUTAM Conf. on Bubble Dynamics and Interfacial Phenomena* (ed. J. R. Blake). Kluwer.

CLIFT, R., GRACE, J. R. & WEBER, M. E. 1978 *Bubbles, Drops, and Particles.* Academic.

CROWE, C. T., TROUTT, T. R. C. & CHUNG, J. N. 1996 Numerical models for two-phase turbulent flows. *Annu. Rev. Fluid Mech.* **26**, 11–43.

DUINEVELD, P. C. 1998 Bouncing and coalescence of bubble pairs rising at high Reynolds number in pure water or aqueous surfactant solutions. *Appl. Sci. Res.* **58**, 409–439.

ERVIN, E. A. & TRYGGVASON, G. 1997 The rise of bubbles in a vertical shear flow. *J. Fluid Engng* **119**, 443–449.

ESMAEELI, A. & TRYGGVASON, G. 1996 An inverse energy cascade in two-dimensional, low Reynolds-number bubbly flows. *J. Fluid Mech.* **314**, 315–330.

ESMAEELI, A. & TRYGGVASON, G. 1998 Direct numerical simulations of bubbly flows. Part 1. Low Reynolds number arrays. *J. Fluid Mech* **377**, 313–345.

ESMAEELI, A. & TRYGGVASON, G. 1999 Direct numerical simulations of bubbly flows. Part 2. Moderate Reynolds number arrays. *J. Fluid Mech.* **385**, 325–358.

FAN, L. S. & TSUCHIYA, K. 1990 *Bubble Wake Dynamics in Liquids and Liquid Solid Suspensions.* Butterworth-Heinemann.

FORTES, A. F., JOSEPH, D. D. & LUNDGREN, T. S. 1987 Nonlinear mechanics of fluidization of beds of spherical particles. *J. Fluid Mech.* **177**, 467–483.

GLOWINSKI, R., PAN, T.-W., HESLA, T. I. & JOSEPH, D. D. 1999 A distributed Lagrange multiplier/fictitious domain method for particulate flows. *Intl J. Multiphase Flow* **25**, 755–794.

HARPER, J. F. 1970 On bubbles rising in line at large Reynolds numbers. *J. Fluid Mech.* **41**, 751–758.

HARPER, J. F. 1997 Bubbles rising in line: why is the first approximation so bad? *J. Fluid Mech.* **351**, 289–300.

HETSRONI, G. 1982 *Handbook of Multiphase Systems.* McGraw-Hill.

HU, H. H. 1996 Direct numerical simulations of flows of solid–liquid mixtures. *Intl J. Multiphase Flow* **22**, 335–352.

ISHII, M & ZUBER, N. 1979 Drag coefficient and relative velocity in bubbly, droplet or particulate flows. *AIChE J.* **25**, 843–855.

JAN, Y. J. 1994 Computational studies of bubble dynamics. PhD dissertation, The University of Michigan.

JOHNSON, A. A. & TEZDUYAR, T. E. 1997 3D simulation of fluid-particle interactions with the number of particles reaching 100. *Comput. Meth. Appl. Mech. Engng* **145**, 301–321.

KARIYASAKI, A. 1987 Behaviour of a single gas bubble in a liquid flow with a linear velocity profile. *Proc. of the 1987 ASME-JSME Thermal Engineering Joint Conf.* ASME, New York, NY, pp. 261–267.

KATZ, J. & MENEVEAU, C. 1996 Wake-induced relative motion of bubbles rising in line. *Intl J. Multiphase Flow* **22**, 239–258.

KOK, J. B. W. 1989 Dynamics of gas bubbles moving through a liquid. PhD dissertation, University of Twente.

LANCE, M. & BATAILLE, J. 1991 Turbulence in the liquid phase of a uniform bubbly air–water flow. *J. Fluid Mech.* **222**, 95–118.

LEGENDRE, D. & MAGNAUDET, J. 1998 Interaction between two spherical bubbles rising side by side. In *Proc. Third Intl Conf. on Multiphase Flow, ICMF'98, Lyon, France.*

LUNDE, K. & PERKINS, R. J. 1998 Shape oscillations of rising bubbles. *Appl. Sci. Res.* **58**, 387–408.

McLAUGHLIN, J. B. 1996 Numerical simulation of bubble motion in water. *J. Colloid Interface Sci.* **184**, 614–625.

MAGNAUDET, J. 1997 The force acting on bubbles and rigid particles. *ASME FED* Summer Meeting, June 22–26 (FEDSM97-3522).

MANGA, M & STONE, H. A. 1993 Buoyancy-driven interactions between two deformable viscous drops. *J. Fluid Mech.* **256**, 647–683.

MIYATA, H. 1996 Time-marching cfd simulation for moving boundary problems. *21st Symp. on Naval Hydrodyn. June 24–28, Trondheim, Norway*, pp. 1–21.

MOORE, D. W. 1965 The velocity of rise of distorted gas bubbles in a liquid of small viscosity. *J. Fluid Mech.* **23**, 749–766.

OKA, H. & ISHII, K. 1999 Numerical analysis on the motion of gas bubbles using level set method. *J. Phys. Soc. Japan* **68**, 823–832.

QIAN, J. 1997 Droplet and flame dynamics in combustion phenomena. PhD dissertation, Princeton University.

RYSKIN, G. & LEAL, L. G. 1984 Numerical solution of free-boundary problems in fluid mechanics. Part 2. Buoyancy-driven motion of a gas bubble through a quiescent liquid. *J. Fluid Mech.* **148**, 19–35.

SADHAL, S. S., AYYASWAMY, P. S. & CHUNG, J. N. 1997 *Transport Phenomena with Drops and Bubbles.* Springer.

SANGANI, A. S. & DIDWANIA, A. K. 1993 Dynamic simulations of flows of bubbly liquids at large Reynolds numbers. *J. Fluid Mech.* **250**, 307–337.

SCARDOVELLI, R. & ZALESKI, S. 1999 Direct numerical simulation of free-surface and interfacial flow. *Annu. Rev. Fluid Mech.* **31**, 567–603.

SCHLÜTER, M & RÄBIGER, N. 1998 Bubble swarm velocity in two-phase flows. *HTD-Vol. 361 Proc. of the ASME Heat Transfer Division, vol. 5, ASME 1998.*

SMEREKA, P. 1993 On the motion of bubbles in a periodic box. *J. Fluid Mech.* **254**, 79–112.

SOKOLICHIN, A., EIGENBERGER, G., LAPIN, A. & LÜBBERT, A. 1999 Dynamic numerical simulation of gas–liquid two-phase flows: Euler–Euler versus Euler–Lagrange. *Chem. Engng Sci.* **52**, 611–626.

SPELT, P. D. M. & BIESHEUVEL, A. 1997 On the motion of gas bubbles in homogeneous isotropic turbulence. *J. Fluid Mech.* **336**, 221–244.

STEWART, C. W. 1995 Bubble interaction in low-viscosity liquids. *Intl J. Multiphase Flow* **21**, 1037–1046.

SUSSMAN, M. & SMEREKA, P. 1997 Axisymmetric free boundary problems. *J. Fluid Mech.* **341**, 269–294.

TAKAGI, S. & MATSUMOTO, Y. 1994 Three-dimensional deformation of a rising bubble. *Proc. German-Japanese Symp. on Mulitphase Flow KfK 5389*, p. 499.

TAYLOR, G. I. 1921 Diffusion by continuous movements. *Proc. Lond. Math. Soc.* **20**, 196–212.

TENNEKES, H. & LUMLEY, J. L. 1972 *A First Course in Turbulence*. MIT Press.

TOMIYAMA, A., SOU, A., ZUN, I., KANAMI, N. & SAKAGUCHI 1995 Effects of Eötvös number and dimensionless liquid volumetric flux on lateral motion of a bubble in laminar duct flow. *Proc. of the 2nd Intl Conf. on Multiphase Flow* 95, Kyoto, Japan.

TRYGGVASON, G., BUNNER, B., ESMAEELI, A., JURIC, D., AL-RAWAHI, N., TAUBER, W., HAN, J., NAS, S. & JAN, Y.-J. 2001 A front tracking method for the computations of multiphase flow. *J. Comput. Phys.* **169**, 708–759.

UNVERDI, S.O. & TRYGGVASON, G. 1992 A front-tracking method for viscous, incompressible, multi-fluid flows. *J. Comput. Phys.* **100**, 25–37.

VAN WIJNGAARDEN, L. 1993 The mean rise velocity of pairwise-interacting bubbles in liquid. *J. Fluid Mech.* **251**, 55–78.

VAN WIJNGAARDEN, L. & KAPTEYN, C. 1990 Concentration waves in dilute bubble/liquid mixtures. *J. Fluid Mech.* **212**, 111–137.

YUAN, H. & PROSPERETTI, A. 1994 On the in-line motion of two spherical bubbles in a viscous fluid. *J. Fluid Mech.* **278**, 325–349.

YURKOVETSKY, Y. & BRADY, J. 1996 Statistical mechanics of bubbly liquids. *Phys. Fluids* **8**, 881–895.